MNRAS **000**, 1–18 (0000) Preprint September 29, 2016 Compiled using MNRAS LATEX style file v3.0

The clustering of galaxies in the SDSS-III Baryon Oscillation Spectroscopic Survey: higher-order correlations revealed by germ-grain Minkowski Functionals

Alexander Wiegand*, Daniel J. Eisenstein
Harvard-Smithsonian Center for Astrophysics, 60 Garden St., Cambridge, MA 02138, USA

September 29, 2016

arXiv:1609.08613v1 [astro-ph.CO] 27 Sep 2016

ABSTRACT

We probe the higher-order clustering of the galaxies in the final data release (DR12) of the Sloan Digital Sky Survey Baryon Oscillation Spectroscopic Survey (BOSS) using the method of germ-grain Minkowski Functionals (MFs). Our sample consists of $410,615$ BOSS galaxies from the northern Galactic cap in the redshift range 0.450–0.595. We show the MFs to be sensitive to contributions up to the six-point correlation function for this data set. We ensure with a custom angular mask that the results are more independent of boundary effects than in previous analyses of this type. We extract the higher-order part of the MFs and quantify the difference to the case without higher-order correlations. The resulting χ^2 value of over $10,000$ for a modest number of degrees of freedom, $O(200)$, indicates a 100-sigma deviation and demonstrates that we have a highly significant signal of the non-Gaussian contributions to the galaxy distribution. This statistical power can be useful in testing models with differing higher-order correlations. Comparing the galaxy data to the QPM and MultiDark-Patchy mocks, we find that the latter better describes the observed structure. From an order-by-order decomposition we expect that, for example, already a reduction of the amplitude of the MD-Patchy mock power spectrum by 5% would remove the remaining tension.

Key words: methods: data analysis – methods: statistical – cosmology: large-scale structure of Universe – cosmology: observations

1 INTRODUCTION

The analysis of cosmic large-scale structure in the distribution of galaxies contributed significantly to establish the current cosmological concordance model. With the increasing degree of perfection of the standard two-point correlation analysis, the related measurements reached unprecedented precision. However, the available and upcoming galaxy redshift survey data (Dawson et al. 2013, 2016; Levi et al. 2013; Laureijs et al. 2011) cannot merely be characterized by its two-point correlation properties. Already the filamentary structure that we see in those surveys indicates that the higher-order correlations play an important role. There have been different approaches to use this information for improving our knowledge about the constituents and evolution of the Universe.

The most direct approach of course is to simply measure the higher-order correlations directly. This has been done for both simulated and observed data starting for early catalogs with Peebles & Groth (1975) and Fry & Peebles (1978). Especially measurements of the three-point function have been standard for recent surveys (Marín 2011; Marín et al. 2013; Slepian et al. 2015) and provide useful complimentary information (Slepian & Eisenstein 2015). For higher orders, however, there are computational and conceptual challenges. On the computational side, increasing the order of the correlation function measured unleashes the curse of combinatorics. Measuring all pairs in current surveys is feasible, for all triangles there are methods to do it (Slepian et al. 2015), but beyond that it becomes increasingly hard. And then, from the conceptual side, even if measuring the full n-point function was possible, it would require modeling and covariances for a large number of data bins. Already for a modest number of bins for each parameter of the n-point function this is a challenge. Therefore, it is worthwhile to consider other approaches that contain information on certain aspects of the higher-order clustering without referring to the full correlation functions.

Since the beginning of large-scale structure analysis, a large number of such methods have been used, including moments of counts in cells, void probability (Stratonovich 1963; White 1979), structure functions on minimal spanning trees, wavelet methods, the genus, etc. Recently also approaches that attempt to bring the higher-order information back into the two-point correlation function through non-linear transforms were used like a logarithmic transformation (Neyrinck et al. 2009, 2011; Wang et al. 2011).

The method (re-)considered in this paper is using Minkowski Functionals. They also also fall into the category of methods

* E–mail:jwiegand@cfa.harvard.edu

© 0000 The Authors

that provide condensed access to higher-order information. This information is encoded in the morphology of the density field. Minkowski Functionals access it by quantifying extended regions of the field through their geometrical properties like volume and surface (see Sec. 2.1). For the construction of these extended regions, two different methods have been widely used in the past[1]:

In the first application of Minkowski Functionals for analyzing large-scale structure in the galaxy distribution in Mecke et al. (1994) (see Buchert (1995) for a short motivation and Schmalzing et al. (1996) for a brief overview), the regions considered were defined by the union of balls around every galaxy location. We shall use the same method, referred to as germ-grain model, here and explain the details in Sec. 2.2. After a couple of applications in the analysis of galaxy and cluster catalogs (Kerscher et al. 1996, 1998, 2001, 1997), the germ-grain model has been less used in recent years.

The second and most popular form of the application of Minkowski Functionals works with extended regions that are defined by iso-contours of the field under investigation. It has been used for the higher-order contributions to the dark matter overdensity field (Platzöder & Buchert 1996; Schmalzing & Buchert 1997; Sahni et al. 1998; Sathyaprakash et al. 1998; Schmalzing et al. 1999; Hikage et al. 2003; Nakagami et al. 2004; Blake et al. 2014; Choi et al. 2013), for the weak lensing shear field (Kratochvil et al. 2012; Petri et al. 2013), for local morphology of cosmic structure (Einasto et al. 2014) and for the morphology of reionization bubbles (Gleser et al. 2006; Yoshiura et al. 2016). Another very active field of recent application is the study of iso-temperature contour maps of the cosmic microwave background (CMB) (Schmalzing & Gorski 1998; Schmalzing et al. 2000; Hikage & Matsubara 2012; Ducout et al. 2013; Modest et al. 2013; Munshi et al. 2013; Planck Collaboration XXIII 2014a; Planck Collaboration XXV 2014b; Planck Collaboration XVI 2016), where Minkowski Functionals helped to establish stringent bounds on the non-Gaussianity of the CMB. So the iso-contour Minkowski functionals are a well established tool in various domains of cosmology.

However, as we shall discuss in Sec. 2.2, the germ-grain model accesses different aspects of the higher-order distribution and can be better suited for the analysis of galaxy redshift surveys. We have demonstrated some of these advantages already in the analysis of the Sloan Digital Sky Survey (SDSS) Data Release seven (DR7) Luminous Red Galaxies (LRGs) in Wiegand et al. (2014).

In the present paper, we concentrate more explicitly on the higher-order aspects of the Minkowski Functionals. To this end, we exploit the analytically known connection to the integrals over higher-order correlation functions. Using direct measurements of the two-point correlation function, we can isolate the contribution of higher-order correlation functions to the Minkowski Functionals. This allows us to quantify the evidence for non-Gaussianity of the galaxy distribution (see Pratten & Munshi (2012) and Codis et al. (2013) for related recent studies of non-Gaussianity with isodensity contour functionals).

The analysis is demonstrated with the final data from the Baryon Oscillation Spectroscopic Survey (BOSS) (Dawson et al. 2013) that is now publicly available within the DR12 of SDSS-III. Being the largest spectroscopic galaxy redshift data set yet observed, it provides an ideal testbed for the analysis and reveals the strong presence of higher-order correlations already at redshifts of ≈ 0.55.

[1] See Aragon-Calvo et al. (2010) for a recent alternative.

We proceed as follows: Sec. 2 recalls the properties of Minkowski Functionals in general and the germ-grain model in particular. We write out the connection of the functionals to higher-order correlations explicitly in 2.3 and lay out in 2.4, how knowing the concrete form allows us to isolate the part of the functionals that is only dependent on higher-orders. We explain the subtleties of a Gaussian reference model in the discrete case in 2.5 and recall the basic properties of our Minkowski code in 2.6.

In Sec. 3 we turn to the description of the SDSS DR12 data used. Sec. 3.1 summarizes the data and mocks we are using. In 3.2, we address issues related to the imperfections in the data, constructing a custom angular mask that defines a high quality region. In 3.3 we turn to the radial distribution of the data and choose the analysis volume and the radial grid. In 3.4 we finally discuss the effect of the regions that can not be accounted for by our custom mask.

Sec. 4 then turns to the core of the analysis. In 4.1 we present the Minkowski Functionals of the mocks and the data and explain how we transform the data to be able to isolate the higher-order only part. This part is then examined in 4.2. In 4.3 we demonstrate that the contributions to this higher-order part range at least up to the 6-point function. To wrap up we discuss in 4.4 an interesting aspects about the galaxy distribution using the base Minkowski Functional to study the volume in extreme voids in the observed field.

We conclude in Sec. 5.

2 MINKOWSKI FUNCTIONALS IN THE GERM–GRAIN MODEL

In this section, we shall provide the basic notions necessary for understanding the quantities we used in our analysis. We summarize some key points already covered in the DR7 analysis paper (Wiegand et al. 2014), but with an emphasis on the crucial points that are the source for common misconceptions.

2.1 Minkowski Functionals

Minkowski Functionals (often called MFs later on) quantify the morphology of extended bodies. They are defined as scalar functionals that map the shape of a body to a set of real numbers. A quite surprising result of integral geometry (Hadwiger 1957) is that any such scalar functional, defined for bodies in Euclidean d-dimensional space, that fulfills some basic requirements (motion invariance, additivity and conditional continuity) can be expressed as a linear combination of $d+1$ base functionals.

There are different choices for the normalization of the base functionals. We will use one where the four MFs that exist for $d = 3$ are denoted $V_0 - V_3$ and related to geometrical properties of the body as follows:

$$V_0 = V \;\; ; \;\; V_1 = \frac{S}{6} \;\; ; \;\; V_2 = \frac{H}{3\pi} \;\; ; \;\; V_3 = \chi \; . \tag{1}$$

Here, V is the volume of the body, S is its surface area, H the integral mean curvature of the surface, and χ the Euler characteristic (the integral Gaussian curvature of the surface).

Instead of using the functionals V_μ directly, we will mainly work with the MF densities v_μ:

$$v_\mu \equiv V_\mu / V_{\rm Survey} \; ; \; \mu \in \{0, \ldots, 3\} \; . \tag{2}$$

Here $V_{\rm Survey}$ is the volume within the survey boundary. In the practical calculation of the v_μ discussed in Sec. 2.6, $V_{\rm Survey}$ is the volume of the region that is more than two ball radii away from our custom angular mask of Fig. 3.

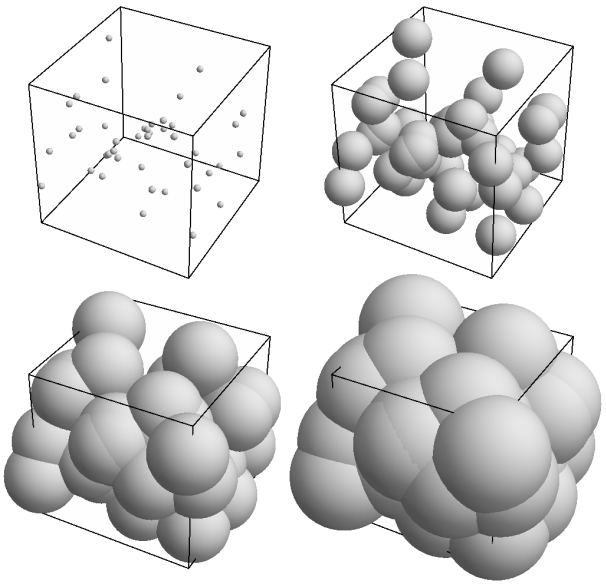

Figure 1. Illustration of the germ-grain procedure to transform a set of galaxies into an extended body. The galaxy positions $\{\mathbf{x}_1, \ldots, \mathbf{x}_N\}$ are surrounded by balls of a common radius R. Then the MFs of the body formed by the union of all the balls are studied as a function of R. The parts of the body outside of the survey region are not taken into account. With increasing R, more and more Balls intersect and a complex structure develops. Through the single and multiple intersections of neighboring balls, it encodes information about the n-point correlation hierarchy. Plot from Wiegand et al. (2014).

2.2 Germ–grain vs. isodensity contours

As mentioned, MFs are only defined for extended bodies. For the analysis of large-scale structure, however, the galaxies are usually treated as points. For points, all quantities in Eq. (1) are, a priori, trivial. For a meaningful analysis of large-scale structure, one therefore has to smooth the point distribution in some manner to define extended regions. The two most popular choices for defining extended regions are:

(i) isodensity contours
(ii) the germ-grain model

The first approach attempts to reconstruct the underlying density field from the observed galaxies and to define the extended bodies as the interior of the surfaces of constant density. The value of this density threshold can then be varied and the functionals are studied as a function of this parameter.

In the second approach, the extended bodies are constructed by surrounding every galaxy (the germ) by an extended body (the grain), which in our case is a ball of a certain radius, and calculating the functionals for the union of all these balls. The diagnostic parameter in this case is the common radius of the balls. Fig. 1 shows how a structured body emerges with increasing radius. Only those parts of the structure are taken into account that lie within the survey boundaries, in Fig. 1 illustrated as a cube.

Even though the basic analysis tool is the same in both cases, the properties of the two approaches are quite different. The isodensity contours, at least in theory, are more directly linked the underlying physical density field, whereas the germ-grain radii are purely diagnostic parameters that merely specify the scale at which the correlations are probed. Regarding the temporal evolution, the MFs for isodensity contours turn out to be relatively independent of the (linear) growth of the density field, if the value of the threshold density is adjusted accordingly. On the germ-grain side, there is no corresponding relabeling and, therefore, as we also shall see below, they depend significantly on the amplitude of the power spectrum. Besides these conceptual differences, there are some technical advantages to the calculation of germ-grain MFs:

(i) The evaluation directly uses the point distribution and does not use a smoothing procedure that is an art by itself. The use of balls does not introduce additional (smoothing) parameters.
(ii) The construction of smooth surfaces can be noisy if the density is low. The rougher smoothing procedure in the germ-grain model on the other hand always constructs some well defined surface.

For both smoothing methods there have been detailed analysis how the values of the measured functionals are related to the parameters of the underlying density distribution. For the germ-grain case we recall this relation in the following section.

2.3 Relation to higher order clustering

Due to the simplicity of the geometrical construction as a union of intersecting balls, it is relatively straightforward to relate the germ-grain MFs to correlation properties of the analyzed point distribution. For the case of a Poisson distribution this has been achieved in Mecke & Wagner (1991), with the only relevant parameter being the density of the random sample. In the presence of structure, the dependence on higher order correlations has first been demonstrated in Mecke et al. (1994). In the following, we shall use the form derived in Schmalzing (1999); Schmalzing et al. (1999) and detailed in the appendix of Wiegand et al. (2014). In these works it has been shown that the ensemble average of the germ-grain MF densities defined in Eq. (2), for the case of balls as grains, can be expressed in an analytic manner as a function of the quantities ϱ_0 and $\overline{V}_\mu$. ϱ_0 is the ensemble average density of the point distribution studied, and the $\overline{V}_\mu$ are the unnormalized modified MFs from the DR7 paper (Wiegand et al. 2014). The analytic relation reads

$$\begin{aligned}
\langle v_0 \rangle &= 1 - e^{-\varrho_0 \overline{V}_0} \,, \\
\langle v_1 \rangle &= \varrho_0 \overline{V}_1 e^{-\varrho_0 \overline{V}_0} \,, \\
\langle v_2 \rangle &= \left(\varrho_0 \overline{V}_2 - \frac{3\pi}{8} \varrho_0^2 \overline{V}_1^2 \right) e^{-\varrho_0 \overline{V}_0} \,, \\
\langle v_3 \rangle &= \left(\varrho_0 \overline{V}_3 - \frac{9}{2} \varrho_0^2 \overline{V}_1 \overline{V}_2 + \frac{9\pi}{16} \varrho_0^3 \overline{V}_1^3 \right) e^{-\varrho_0 \overline{V}_0} \,, \qquad (3)
\end{aligned}$$

and provides the implicit definition of the $\overline{V}_\mu$. In the rest of the paper we will drop the explicit ensemble averaging brackets and use $v_\mu \equiv \langle v_\mu \rangle$ as a shorthand, as we never refer to the MF density of one individual realization. We discuss this aspect in more detail in Sec. 2.6.

For a Poisson distribution, the $\overline{V}_\mu$ are simply the MFs $V_\mu(B)$ of the balls of common radius R that we use to obtain extended bodies:

$$\begin{aligned}
V_0(B) = \frac{4\pi}{3} R^3 \;\; ; \;\; V_1(B) = \frac{2}{3}\pi R^2 \;\; ; \\
V_2(B) = \frac{4}{3} R \;\; ; \;\; V_3(B) = 1 \,. \qquad (4)
\end{aligned}$$

In the Poisson case Eq. (3) reduces to the result of Mecke & Wagner (1991). For a point distribution with structure, the $\overline{V}_\mu$ are modified by weighted integrals of the dimensionless higher-order connected

correlation functions ξ_n. This modification is what we are interested in in this paper. It is convenient to define it as a multiplicative dimensionless correction to the Poisson value, i.e. to study the quantities

$$\eta_\mu \equiv \overline{V}_\mu / V_\mu (B) \ . \tag{5}$$

We will refer to η_μ as the modified MFs. They can be easily obtained from the quantities we measure, i.e. the average densities v_μ, by inverting Eqs. (3):

$$\begin{aligned}
\eta_0 &= -\frac{1}{\varrho_0 V_0} \ln(1-v_0) \ , \qquad (6)\\
\eta_1 &= \frac{1}{\varrho_0 V_1} \frac{v_1}{(1-v_0)} \ ,\\
\eta_2 &= \frac{1}{\varrho_0 V_2} \left(\frac{v_2}{(1-v_0)} + \frac{3\pi}{8} \frac{v_1^2}{(1-v_0)^2} \right) \ ,\\
\eta_3 &= \frac{1}{\varrho_0 V_3} \left(\frac{v_3}{(1-v_0)} + \frac{9}{2} \frac{v_2 v_1}{(1-v_0)^2} - \frac{9\pi}{8} \frac{v_1^3}{(1-v_0)^3} \right) \ .
\end{aligned}$$

In the analysis below, we will mainly use these modified MFs instead of the densities v_μ, as they are more directly related to the correlation properties of the point distribution via (7). From Schmalzing (1999); Schmalzing et al. (1999); Wiegand et al. (2014) the relation of η_μ to the correlations of order $n+1$, ξ_{n+1}, is of the form

$$\begin{aligned}
\eta_\mu (R, \varrho_0) &= 1 + \sum_{n=1}^{\infty} \frac{(-\varrho_0)^n}{(n+1)!} \int \mathrm{d}^3 x_1 \ldots \mathrm{d}^3 x_n \qquad (7)\\
&\quad \times \xi_{n+1}(0, \mathbf{x}_1, \ldots, \mathbf{x}_n) \frac{V_\mu (B \cap B_{\mathbf{x}_1} \cap \cdots \cap B_{\mathbf{x}_n})}{V_\mu (B)} \ .
\end{aligned}$$

with $V_\mu (B \cap B_{\mathbf{x}_1} \cap \cdots \cap B_{\mathbf{x}_n})$ being simply the MFs of the *intersection* of $n+1$ balls. $B = B(R)$ denotes a ball around the origin and $B_{\mathbf{x}} = B_{\mathbf{x}}(R)$ a ball around the point $\mathbf{x}$. In our model all intersecting balls have the same radius R. For general germ-grain models, this is not a necessary requirement. One could imagine to increase the weight of some points by assigning them larger radii than other points. Using elliptic or even more irregular grains would also be possible. However, this would complicate the interpretation as we expect that it would lead to a more complicated relation of the functionals to the correlation hierarchy than the one of Eq. (7).

The advantage of the η_μ of being more directly related to the correlation properties is counterbalanced by an increase in the error. In Wiegand et al. (2014) we found weaker constraints when using the $\overline{V}_\mu$ as compared to the v_μ. The main reason for this is the additional error that is introduced by removing the exponential suppression $e^{-\varrho_0 \overline{V}_0} = (1-v_0)$ from $v_1 - v_3$ in (3). For η_1, for example,

$$\frac{\delta\eta_1}{\eta_1} = \frac{\delta v_1}{v_1} + \frac{\delta v_0}{(1-v_0)} \ .$$

So the relative error for the fraction of the volume not covered by any ball enters also for the higher functionals. This spoils to some extent the good precision that can be obtained for $v_1 - v_3$, because v_0 has to be measured in the full volume and $v_1 - v_3$ only on the surface. Especially for small $1 - v_0$ it becomes costly to determine v_0 well enough. We will therefore restrict our analysis of the η_μ to parameter regions where $1 - v_0$ is larger than ≈ 0.01.

2.4 Density dependence

The modified MFs η_μ of Eq. (7) not only depend on our diagnostic parameter, i.e. the radius R of the balls that we are using to smooth the galaxy distribution, but also on the sample density. The rather complicated R dependence is entirely encoded in the weight functions $V_\mu (B \cap B_{\mathbf{x}_1} \cap \cdots \cap B_{\mathbf{x}_n}) / V_\mu (B)$ in the integrals over correlation functions. The dependence on the mean density of the galaxy sample ϱ_0, however, is of an easier form. It is a simple power series in ϱ_0

$$\eta_\mu = \sum_{n=0}^{\infty} \frac{c_{\mu,n+1}}{(n+1)!} (-\varrho_0 V_0(B))^n \tag{8}$$

with coefficients $c_{\mu,1} = 1$ and

$$\begin{aligned}
c_{\mu,n+1}(R) &= V_0^{-n}(B) \int \xi_{n+1}(0, \mathbf{x}_1, \ldots \mathbf{x}_n) \times \qquad (9)\\
&\quad \frac{V_\mu (B \cap B_{\mathbf{x}_1} \cap \cdots \cap B_{\mathbf{x}_n})}{V_\mu (B)} \mathrm{d}^3 x_1 \ldots \mathrm{d}^3 x_n
\end{aligned}$$

that contain all of the radius and correlation function dependence. $V_0(B)$ is the volume of a ball B of radius R. We choose to define the second index of $c_{\mu,n+1}$ such that it directly corresponds to the order of the integrated correlation function.

The formal split into ϱ_0 dependence and correlation function dependence in Eq. (8) allows us two things: First, we can remove the Poisson part and the part that depends on the two-point correlation function, if we measure the sample density and the two-point correlations independently. This leaves us with a quantity

$$\eta_\mu^h (R, \varrho_0) \equiv \sum_{n=2}^{\infty} \frac{c_{\mu,n+1}(R)}{(n+1)!} (-\varrho_0 V_0(B))^n \tag{10}$$

that only includes higher-order contributions. This will prove the significance of their contribution to the MFs in Sec. 4.2. Second, we can extract the integrals over correlation functions by fitting a polynomial to the density evolution of $\eta_\mu(\varrho_0)$. This allows to define a fitting formula for the form of the MFs in the SDSS by giving the values and covariances of the coefficients $c_{\mu,n}(R)$. We shall use this in Sec. 4.3.

We close with the remark that, in general, a finite number of coefficients is not sufficient to describe the full shape of a power series of the sort (8). For cooked up point distributions with small ξ_n, but a single large ξ_m at some higher m, giving only the lower coefficients will not determine η_μ well. For the assumed structure of the Universe as the product of standard structure formation, however, we find that the coefficients $c_{\mu,n}$ are well behaved and the series η_μ converges reasonably well (see Sec. 4.3).

2.5 Example: Gauss-Poisson clustering

In order to illustrate the relations (7), let us consider the simplest non-trivial case. In analogy with the continuous case, one can define a Gaussian point distribution by the absence of all higher-order connected correlation functions. In this case the hierarchy of correlations in (7) is truncated after the linear term and we have

$$\eta_\mu = 1 - \frac{\varrho_0}{2} \int \mathrm{d}^3 x_1 \xi_2(0, \mathbf{x}_1) \frac{V_\mu (B \cap B_{\mathbf{x}_1})}{V_\mu (B)} \ . \tag{11}$$

The weight functions $V_\mu (B \cap B_{\mathbf{x}_1}) / V_\mu (B)$ are non-zero only for the range of $\mathbf{x}_1$-values for which the balls intersect. For a coordinate system centered around the origin, i.e. the center of B, the $\mathbf{x}$-values therefore lie in a sphere of radius $2R$. A configuration of balls of radius R therefore probes the correlation function up to a scale $2R$. We shall therefore plot the radial dependence as a function of the diameter $D = 2R$ instead of the radius. For isotropic

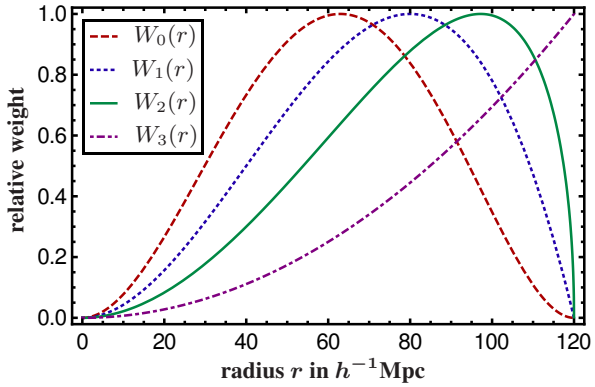

Figure 2. Form of the integration windows $W_\mu(R,r) \equiv V_\mu(R,r)/V_\mu(R)\,r^2$ of Eq. (12), for a ball radius of $R = 60h^{-1}$Mpc. All functions have been normalized to their maximal value. The functionals of higher index μ probe the correlation function at larger distances. (same plot already in Wiegand et al. (2014))

correlations (11) becomes

$$\eta_\mu = 1 - 2\pi\varrho_0 \int_0^{2R} \frac{V_\mu(R,r)}{V_\mu(B(R))}\xi_2(r)\,r^2\mathrm{d}r\ . \tag{12}$$

The shape of the weights $V_\mu(R,r)$ is shown in Fig. 2.[2] Let us just recall that the weights are such that η_0 and η_3 have a particularly interesting form. η_0 directly contains the amplitude of fluctuations on the scale of the balls $\sigma(R)$,

$$\eta_0 = 1 - \frac{\frac{4\pi}{3}R^3\varrho_0}{2}\sigma^2(R)\ , \tag{13}$$

and η_3 is a simple integral over the two-point function

$$\eta_3 = 1 - 2\pi\varrho_0 \int_0^{2R} \xi_2(r)\,r^2\mathrm{d}r\ , \tag{14}$$

which could therefore be recovered from the derivative of η_3.

Let us pause here and elaborate a bit on the Gauss-Poisson process as such (see Kerscher (2001) for a more complete discussion of what follows). It is tempting to think of the truncated quantities (12) as being the MFs of a point distribution that represents the Gaussian limit of an actual point distribution that has higher-order correlations. However, in general there will not be a Gauss-Poisson point process that actually realizes these MFs, as in order for a Gauss-Poisson process to exist, ξ_2 and ϱ_0 have to fulfill certain conditions.

Already in the continuum case, the clustering amplitude is limited by the fact that the matter density can only be positive. The density distribution, therefore, is in any case only approximated by a Gaussian. This approximation of course is, excellent for early times and large scales, but when matter fluctuations $\sigma(R)$ grow too large it breaks down. This is also the point where higher-order correlations become important.

In the same manner, the clustering amplitude of a Gauss-Poisson point process is limited. In this case, however, also the mean density of the point sample ϱ_0 plays a role. For low enough density a thinning of the point distribution goes to an approximated Poisson distribution. This effect can compensate larger fluctuations and it can be shown (Kerscher 2001) that the corresponding constraint is

$$\sigma^2(A) \leqslant \frac{1}{V_A\varrho_0} = \frac{1}{\overline{N}_A} \tag{15}$$

where $\sigma^2(A)$ are the fluctuations in the number density of cells A stemming from structure ($\sigma^2 = \overline{N}_A + \overline{N}_A^2\sigma^2(A)$ are the full fluctuations including the Poisson term), V_A is the volume of one of these cells, and $\overline{N}_A$ the mean number of particles in such a cell. This constraint has two interesting implications: First, we can already tell from the amplitude of the two-point function if the field will have a significant amount of higher order clustering. When we evaluate (15) for the structure that we measure in the BOSS galaxies, we find that the constraint actually is violated. Second, to study the Gaussian limit on large scales it is not sufficient to simply increase the domain size (the ball size in our case). In some cases, where the fluctuations on a region decay faster than its volume the constraint indicates that the structure for larger cells becomes more Gaussian. In general, however, one will have to reduce the number density. In the continuous case, by smoothing over larger and larger regions, the amplitude of the fluctuations between these regions decreases and the Gaussian approximation becomes better and better. In the discrete case, the analogous coarse graining procedure involves a subsampling of the density field. In the same way that the number of regions is reduced in the continuous case when averaging the density over larger cells, individual points of the downsampled point distribution represent larger regions. We will demonstrate this effect in Sec. 4.1 where we show the MFs for a couple of densities. The lower this density becomes, the better the Gaussian model fits.

In addition to the requirement (15), Kerscher (2001) also showed that the correlation function of a Gauss-Poisson point process has to satisfy

$$\varrho_0 \int_A d^3x\,\xi_2(|\mathbf{x}|) \leqslant 1 \tag{16}$$

and cannot be negative

$$\xi_2(r) \geqslant 0\ \ \forall r \in R\ . \tag{17}$$

Any violation of (15) – (17) already implies the existence of higher-order correlations ξ_n with $n \geqslant 3$.

We note finally that the condition (15) prevents (13) and therefore the volume fraction v_0 in (3) from becoming negative. So we could have derived a similar constraint on a Gauss-Poisson process from the requirement that $0 \leqslant v_0 \leqslant 1$.

2.6 Practical realization and the Chipmink code

The procedure we use to measure the functionals is the same as in the DR7 analysis (Wiegand et al. 2014). As the quantities that are related to the hierarchy of correlation functions via (3) are, strictly speaking, the ensemble averages of the MF densities v_μ, we approximate these averages by creating randomly subsampled realizations of the point distribution and averaging over their MF densities. Mathematically speaking there is no guarantee that these averages should converge to those of an ensemble of independent realizations (see also Kerscher et al. (2000)), but practically the

[2] The equations for the $V_\mu(R,r)$ and their Fourier transforms can be found in Wiegand et al. (2014) (in the Fourier form of W_2 in Eq. (16) there is a typo: the prefactor of the integral should be $8/3 \times R^3/k$ instead of $2/3 \times R/k$).

procedure is working quite well. For studies on small scales one could in principle use subfields of the full survey as independent realizations and perform an average that is then more likely to converge (even though it also requires the assumption of ergodicity and is only valid approximately as neighboring regions are not completely independent). For the scales that we are interested in, however, there is only one realization of the survey and therefore we use the subsampling. For details on how we generate the samples see the end of Sec. 3.3.

The calculation of the v_μ for a given downsampled realization is performed by CHIPMINK (Code for High–speed Investigation of Partial Minkowski Functionals), introduced in the DR7 paper (Wiegand et al. 2014). In a first step, it generates neighbor lists for every galaxy in the sample. Galaxies are considered as neighbors if they are closer than twice the maximal radius of the balls. To determine v_1-v_3, the code considers galaxies that are more than $2R$ away from the boundary. Using the list of neighbors the code calculates the uncovered surface, integrated mean curvature and Euler characteristic of the ball put around the galaxy. These partial functionals are then summed to give the global v_μ. The volume used for obtaining the densities from the summed $V_1 - V_3$ is the effective part that is more than $2R$ away from the boundary.

For the volume functional v_0 another set of neighbor lists is generated that contains all galaxies within $2R_{max}$ around points from a random sample filling the same volume as the data, but also eventual holes in the data that are not treated as internal boundaries. Around each primary random point we generate $10,000$ random points in spheres of increasing radius $0 < R < R_{max}$. The volume fraction covered by the balls is then estimated by counting the fraction of the secondary randoms that have a distance of less than R to any of the galaxies in the neighbor list of the primary random point.

As compared to the DR7 code, we made a couple of enhancements. Besides improved memory management, the code can now handle boundaries of arbitrary shape in ra-dec. It can use data with non-constant density, uses a larger fraction of points for radii smaller than R_{max}, and samples the $R - \varrho_0$-plane more efficiently than the earlier version. We plan to make also the current version publicly available.

3 DATA REDUCTION

Having completed the discussion of the methods, we now turn to a description of the data. The galaxy sample we are analyzing was observed by the Sloan Digital Sky Survey (SDSS) (York et al. 2000) using the 2.5-meter Sloan Telescope (Gunn et al. 2006). Photometric data used for target selection was obtained using a drift-scanning mosaic CCD camera (Gunn et al. 1998) and information on the camera, photometry and photometric pipeline can be found in Fukugita et al. (1996); Lupton et al. (2001); Smith et al. (2002); Pier et al. (2003); Padmanabhan et al. (2008); Doi et al. (2010). All the photometry was re-processed and released in the eighth data release (Aihara et al. 2011). Based on the so obtained target catalog, the spectroscopic redshifts are taken by the spectrographs described in Smee et al. (2013). The final step of spectroscopic data reduction and redshift determination is presented in Bolton et al. (2012).

The data analyzed here is contained in the twelfth data release (DR12) (Alam et al. 2015) of SDSS data and was obtained during the third stage of SDSS (Eisenstein et al. 2011) within the Baryon Oscillation Spectroscopic Survey (BOSS) (Dawson et al. 2013). It is described in detail in Reid et al. (2016). The full data set consists of the spectroscopic redshifts of 836,347 galaxies. The area probed is divided in a northern and a southern part and two different target redshift ranges. For our analysis we use the largest contiguous part of the survey, which is the northern CMASS sample. Given the technical progress in the boundary treatment of our code, mentioned in Sec. 2.6, it would now also be possible to use it for the combined sample analyzed in Alam et al. (2016).

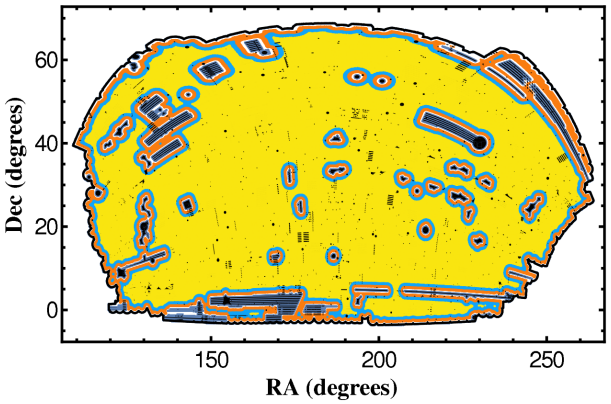

Figure 3. External and internal boundaries. In black are regions excluded by one of the four veto masks we consider. In blue the subset of the black regions that we chose to define our boundary. In orange, light blue and yellow a projection of the regions 18, 36 and $54h^{-1}\mathrm{Mpc}$ away from the nearest boundary.

The mock catalogs we are using for estimating errors and covariances were constructed using two different methods. One is based on the quick particle mesh technique (QPM) described in White et al. (2014) and the other one is a hybrid method (Kitaura et al. 2014) which employs what the authors call "augmented" second-order Lagrangian perturbation theory. It was used for generating the MultiDark(MD)-Patchy mocks (Kitaura et al. 2016). We shall work with both mock catalogs in our analysis, but concentrate on the MD-Patchy mocks.

3.1 The SDSS DR12 CMASS data and mock catalogs

For taking the data of the northern CMASS sample, $685,698$ objects were targeted over an area of $7,429\,\mathrm{deg}^2$. Out of these, $607,357$ turned out to be galaxies and obtained redshifts from good BOSS spectra (Reid et al. 2016). They are distributed over $6,934\ \mathrm{deg}^2$. Their redshifts range approximately from 0.4 to 0.8. The central region of redshift 0.43-0.70 that is used in most of the CMASS analysis (see e.g. Cuesta et al. (2016)) contains $568,776$ galaxies.

The MD-Patchy and QPM mock catalogs are constructed such that they trace the number density of the data. They are available for the central range of 0.43-0.70. Their angular distribution fills the full survey geometry. For matching the angular distribution of the data as well, regions of bad data quality or missing observations can be masked out. The QPM mocks contain on average $651,316$ galaxies. After application of the full veto mask the average number is $576,517$. For the MD-Patchy mocks, the unmasked number of galaxies is $674,880$ and the masked one $591,192$.

Our custom radial selection of a redshift range of $z = 0.450 - 0.595$, explained in Section 3.3, reduces the number of galaxies that we use to $410,615$.

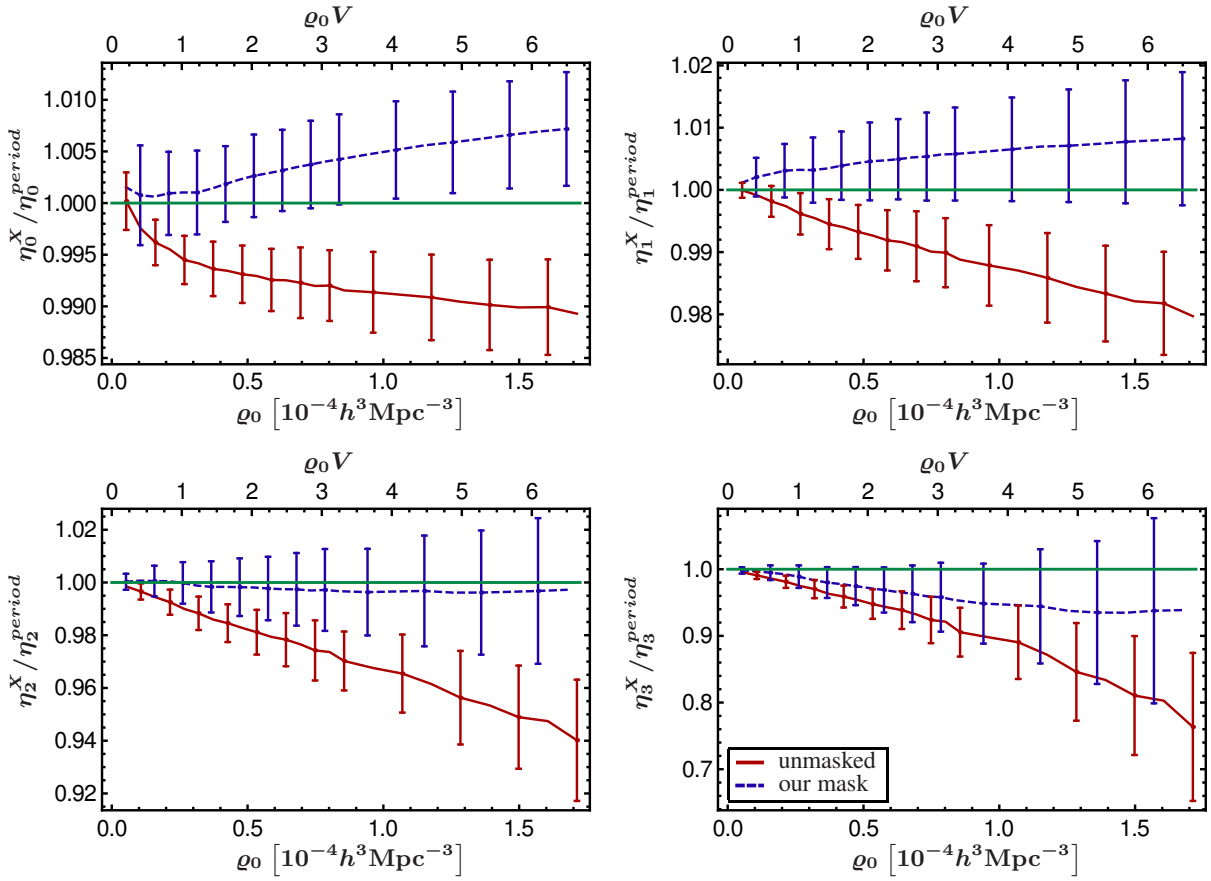

Figure 4. Ratios $\eta_\mu^{uncorr}(\varrho) / \eta_\mu^{period}(\varrho)$ (solid line) $\eta_\mu^{corr}(\varrho) / \eta_\mu^{period}(\varrho)$ (dashed line) for a diameter of $42h^{-1}$Mpc. $\eta_\mu^{uncorr}(\varrho)$ is determined for the MD-Patchy galaxies after applying the full veto mask that includes all seven effects discussed in the text. Only the outer boundaries are taken into account when calculating the v_μ. $\eta_\mu^{corr}(\varrho)$ uses the same galaxies, but includes also the inner boundaries chosen in Fig. 3. $\eta_\mu^{period}(\varrho)$ are derived from cubic periodic boxes without any boundary. The deviation is largest for the functionals probing the largest scales η_3 and reduces to a sub-percent deviation for η_0. For η_2 and η_3 our mask correction is most effective and getting $\eta_\mu^{period}(\varrho)$ within the error bars of $\eta_\mu^{corr}(\varrho)$. For smaller diameter than $42h^{-1}$Mpc, the relative deviation is less important.

3.2 Correcting for the survey geometry

In order to compare the data to the galaxy samples created in the mock catalogs, it would be sufficient to calculate the MFs for the masked mocks and the data. However, ideally we would like to derive quantities that are independent of effects of the survey boundary. This is not necessary for the direct comparison, but desirable for later comparison of the data with other simulations without having to apply the survey mask to them. When estimating the correlation function, the effect of boundaries (inner boundaries such as holes as well as the outer boundary) can be taken into account by using random samples with the exact same boundaries as the data. The excess of data over random pairs in a given bin is then solely due to structure.

In the case of the MFs, unfortunately there is no simple analogue to this approach. We tried to correct the MFs of the masked mocks with the MFs of a random distribution and the same mask. A comparison with the unmasked mocks showed that this correction is not effective in the MF case. In order to minimize the influence of boundaries, we therefore choose to restrict our analysis to regions with good data quality. This is achieved by using only galaxies that are more than $2R$ away from the closest boundary, where R is the common radius of the balls around every galaxy (see Sec. 2.2). Of course, especially for large R, this reduces the volume probed and so the number of galaxies that can be used. We therefore have to find a compromise as to which boundaries we include and which we can ignore without affecting the result too much.

As discussed in detail in Reid et al. (2016), there are at least seven different effects that lead to bad or missing data. For each effect there is a veto mask that can be used in the correlation function analysis. The effects are:

- The central bolt obscures the center of the plate
- Ly–α targets are given priority in fiber assignment
- No observations around bright stars
- No observations around bright objects
- Non-photometric conditions
- Spectra with bad seeing
- Spectra degraded by extinction

The regions obscured by the first three effects are quite small individually, but relatively evenly distributed over the sky. Including them, and especially the $2R$ region around them, would reduce the usable area by a large amount, so we can not correct for their effect. The fourth effect is also present all over the sky, however, the

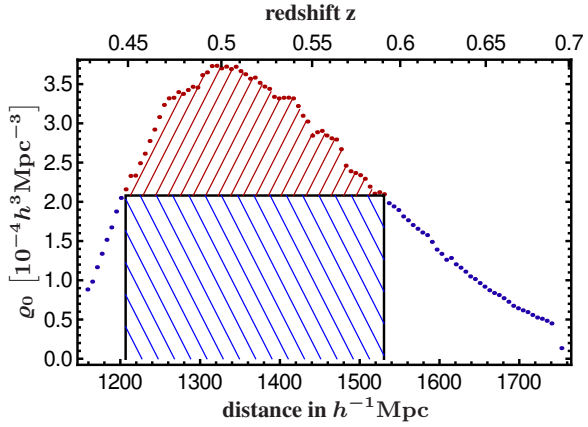

Figure 5. Radial selection: The full redshift range analyzed is $z = 0.450 - 0.595$. The points indicate the minimal value of the density of the 1000 QPM mocks in the respective bin. The reference density with respect to which we define our downsampling is $2.08 \times 10^{-4} h^3\mathrm{Mpc}^{-3}$. This combination of reference density and redshift range maximizes the number of downsampled galaxies in the boxed blue shaded region. We also use the points above the reference density by downsampling always from the full density.

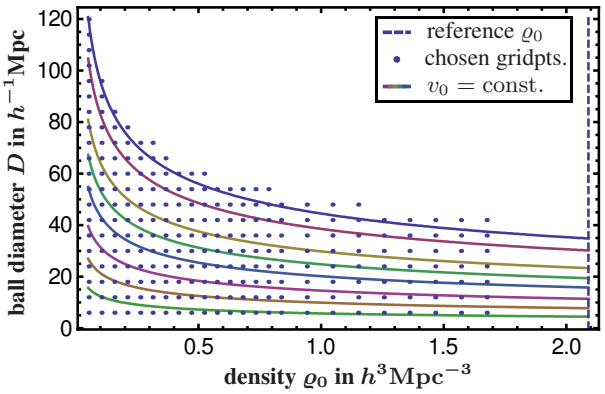

Figure 6. Choice of points in the D-ϱ_0-space. For the smaller diameters there are 24 density points, for the largest diameter used in the analysis $66h^{-1}\mathrm{Mpc}$, there are 7. The lines of constant v_0 are calculated for a Poisson point process and correspond to $\{0.99, 0.95, 0.75, 0.55, 0.35, 0.15, 0.05, 0.01\}$ from top to bottom.

obscured regions have a wide range of sizes. Therefore we can exclude the largest ones.

The combination of the lower four masks is shown as the black regions in Fig. 3. Of those regions we select those with an area on the sky of more than about $0.8\,\mathrm{deg}^2$. We densely sample these regions and their boundaries with points that are shown in blue. These are used to determine the distance of a galaxy from the nearest boundary. The projected holes created by ball diameters $2R$ of 18, 36 and $54\,h^{-1}\mathrm{Mpc}$ are shown as the regions not filled by orange, blue and yellow color. At these diameters the effective volume left is 75%, 57% and 42%, respectively. For the largest scales probed of $120h^{-1}\mathrm{Mpc}$, only 8% remains.

As the mask we constructed does not take into account all imperfections, we have to test the extent to which the result still depends on the survey boundaries. In order to study this, we removed the galaxies from the mocks that fall into one of the seven masks described above. Then we determined the distance of the remaining galaxies from our boundaries that are shown in Fig. 3. We calculated their germ-grain MFs and those of the galaxy in the corresponding cubic mocks periodically wrapped to remove any boundary. The resulting comparison is shown in Fig. 4. It also contains the case where we use the full veto mask to remove the unobserved galaxies, but only take the outer boundaries into account in the calculation of the MFs. We find that our custom mask greatly improves the match with the boundaryless case as compared to not taking inner boundaries into account. After the correction the periodic MFs are now within the error bars of the sky MFs.

The sky values of η_0 in Fig. 4 have been corrected for a systematic 0.5% offset from the periodic case. We shall apply the same correction throughout the rest of the paper. As the offset has been derived from a comparison of the sky mocks to the periodic mocks, one could think of using the deviations of Fig. 4 to apply density and scale dependent corrections to both the sky mocks and the data, to empirically remove the effect of the boundary. We decided not to apply this correction as it would make the results for the MFs of the data completely dependent on this particular set of mocks.

From Fig. 4, we also see that our correction is largest for the fourth functional η_3 and least important for η_0. This reflects the property of the integration kernel of Fig. 2. With increasing index μ, the functionals probe larger and larger scales and are hence more sensitive to the large scale boundary effects we removed.

3.3 Radial selection and density binning

In addition to the angular selection, we also apply some radial cuts. As described in Sec. 2.4 we want to study the MFs of the galaxy distribution as a function of ball radius, but also sample density. A controlled variation of sample density requires a roughly constant density throughout the sample. Otherwise the summation of partial MFs (see Sec. 2.6) from different regions of the survey would combine v_μ values effectively measured at different densities, removing the clear distinction between the ϱ_0 and the ξ_n dependence in Eq. (3).

To generate a homogeneous sample we downsample the density to a common value for all radial shells. The concept is shown in Fig. 5. There, we plot the binned density distribution of the QPM mocks. For each bin we show the minimum of the 1000 QPM mocks. Using this density distribution, we choose a reference density such that the number of points in the constant density region of the considered redshift range is maximal. This density is $2.08 \times 10^{-4} h^3\mathrm{Mpc}^{-3}$ and corresponds to 296,738 galaxies. The total number of galaxies in this redshift range is 410,615. As we used the minimum of all mocks, we can be sure that we can downsample from this reference density and obtain the same constant density for every single mock realization.

The sampling points in radius and density that we used are shown in Fig. 6. For ball diameters up to $42h^{-1}\mathrm{Mpc}$, there are 24 density points ranging from 2.5% to 80% of the reference density. For diameters above $42h^{-1}\mathrm{Mpc}$ we decrease the maximal density and therefore the number of density points. The reason for this is two-fold: First, as discussed in Sec. 2.3, for very small fractions of uncovered volume (i.e. large radius and/or high density), the precision of the determination of v_0 is no longer high enough to give reasonable error bars for the derived quantities η_μ. Second, the runtime is much worse if the galaxies have a large numbers of neighbors. The density cutoff in Fig. 6 is therefore roughly chosen along the lines of constant v_0. Fig. 6 includes these lines for the Pois-

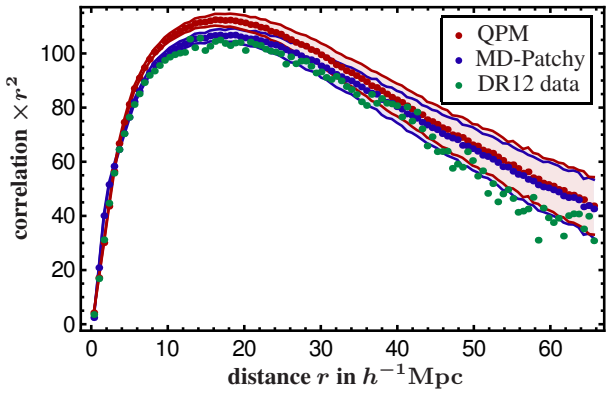

Figure 7. Average correlation functions for the QPM and MD-Patchy mocks compared to the correlation function of the DR12 data. The shaded region shows the 1σ scatter of the mocks.

son case, which we used for a first estimate of reasonable density ranges.

From the range of diameters shown in Fig. 6, we choose $18h^{-1}$Mpc to $66h^{-1}$Mpc for our analysis. For smaller scales than $18h^{-1}$Mpc we expect to pick up too much effects from the ignored holes in the survey and for larger scales than $66h^{-1}$Mpc, the volume far enough from the boundary becomes too small.

For our independent measurement of the correlation functions of the data and the mocks, we chose to use those regions that are more than $36h^{-1}$Mpc away from the closest boundary that we treat. The structure that we measured for these regions is shown in Fig. 7.

The concrete Monte Carlo procedure we use is then to randomly select galaxies from the full number of galaxies in our redshift range (and *not* a pre-downsampled reference density as in the DR7 paper) for each $D - \varrho_0$-point of the grid in Fig. 6, to obtain a sample with the constant target density in each radial bin. We then calculate the MFs for this configuration. We repeat the random selection and average the resulting MFs over these different realizations of the subsampled point distribution. The number of realizations is largest for the smallest densities and ranges from 617 for a fraction of 2.5% to 10 for a fraction of 80%.

3.4 Weights

In addition to the regions that could not be observed or had bad data quality and that therefore had to be masked out, there are also imperfections in the rest of the observed survey volume. Even though the completeness of the survey is high, see Reid et al. (2016), there are still galaxies that have not obtained robust redshifts (no-z). In addition due to the physical size of the fibers of the spectrograph, galaxies separated by less than $62''$ can not be observed simultaneously (close pairs). In the correlation function analysis, these holes are accounted for by upweighting nearby galaxies. In our case this can not be done as easily. In principle one could use imaging data for the angular position and the redshift of nearby galaxies to mimic the procedure in the correlation function case and fill in the holes. However, as we are already ignoring a large number of holes and looking at relatively large scales, we decided not to take these holes into account and to mask them in the mocks consistently.

However, we include another class of weights correcting for spurious density fluctuations due to stellar density and seeing. For the correlation function analysis, these have been combined into a systematic weight (see Reid et al. (2016)). We use this systematic weight to adjust the probability of selecting a galaxy when we downsample to a given target density. As the modifications are below 10% and not factors of 2 to 7 as in the case of the no-z and close pairs weights, the fluctuations can be accounted for relatively easily by this procedure.

4 NON-LINEAR CLUSTERING AS SEEN BY THE MINKOWSKI FUNCTIONALS

In this section we first present the measured values for the observables v_μ introduced in Sec. 2.3. We study their radial and density dependence based on the MD-Patchy mocks. Then we turn to the analysis of the higher-order contributions. For this analysis, we need the η_μ that are obtained from the measured v_μ through Eqs. (6). From the η_μ we can then simply subtract the two-point part of the expansion (7) to extract the η_μ^h part (10) that only depends on higher orders. We will see that it contributes significantly to the full η_μ. Finally we analyze the coefficients $c_{\mu,n}$ of (7) order by order and compare them to correlation function integrals.

4.1 The functional densities measured

As mentioned in Sec. 2.6, the quantities calculated by CHIPMINK are the the MF densities v_μ. Their dependence on the ball diameter is shown in Fig. 8 and based on the mean of 30 MD-Patchy realizations. We only used 30 mocks in this case because Fig. 8 is mainly for illustration and the large range of diameters is not optimal for the evaluation of the η_μ as discussed at the end of Sec. 2.3. In order to illustrate also the density dependence, we plot 12 different densities ranging from 2.5% to 80% of our reference density of $2.08 \times 10^{-4} h^3 \mathrm{Mpc}^{-3}$ (the same density points as in Fig. 6, however with an increased maximal radius). For the most extreme cases of 2.5% and 80%, we also plot the MFs of a Poisson point process as dashed lines. For the high density case, the functionals for the mocks are clearly non-Poissonian, whereas in the low density case the downsampling erased already a lot of the structure and the difference to a Poisson sample is less important.

Let us qualitatively describe the difference for the Euler characteristic v_3 ($v_3 = \chi = K - H + C$). The faster drop of the functional with structure indicates that the individual balls aggregate earlier, which reduces the number of independent components K faster than for the Poisson case. Then the holes H in the union of multiple balls prevail up to larger radii and in the end there are less cavities C but at larger radii.

For our quantitative analysis in Sec. 4 we will mainly use the modified MFs η_μ, Eq. (7). Therefore, we use Eqs. (6) to transform from the initial observables $v_\mu(\varrho_0, R)$ to $\eta_\mu(\varrho_0, R)$. Fig. 9 shows the dependence of the η_μ on the ball diameter for the same densities as in Fig. 8, but now for 900 MD-Patchy mocks. In these plots the convergence of the Functionals to those of the Poisson point process with decreasing sample density is more visible than in Fig. 8. However, given the small error bars, even for the lowest density of $5.2 \times 10^{-6} h^3 \mathrm{Mpc}^{-3}$ the structure is well detected.

The differing number of radial points for different densities illustrates our grid of points sampling the $D - \varrho_0$ plane of Fig. 6. For the highest density, 7 radial bins of $\delta R = 3h^{-1}$Mpc are possible until the survey volume is significantly filled, for the lowest density there are 20 bins (of which only the first 15 are shown here).

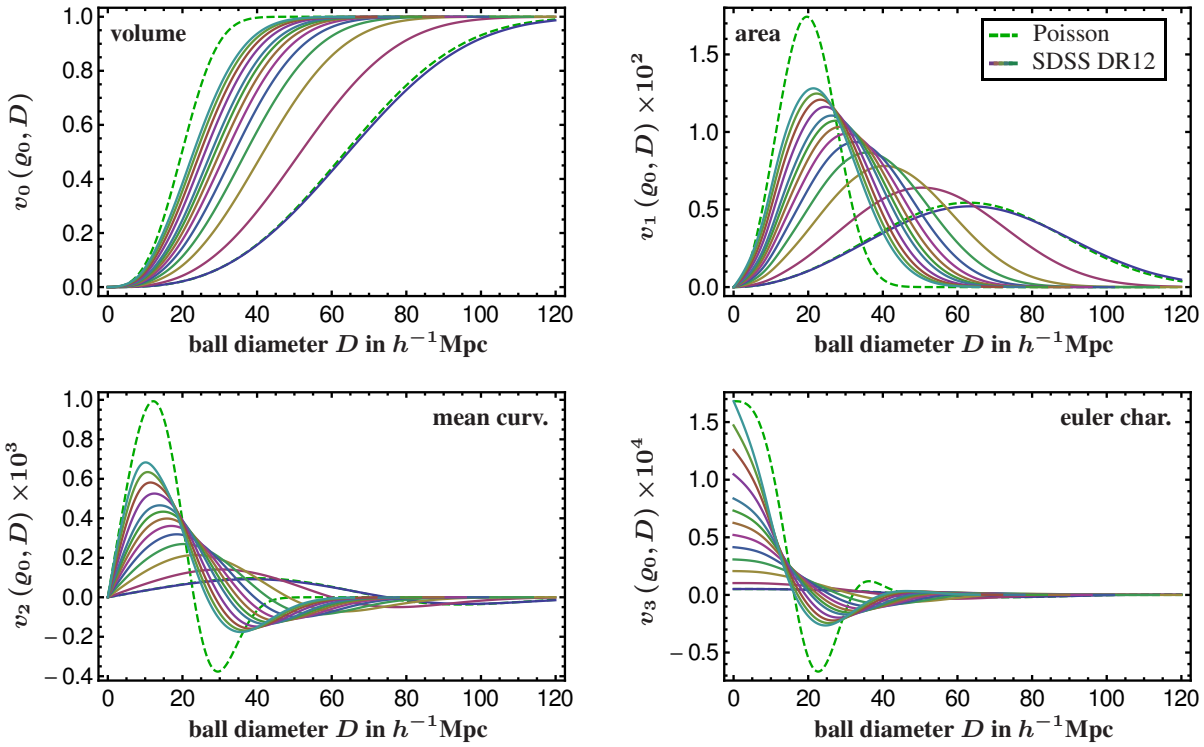

Figure 8. MF densities v_μ from Eq. (3) of the SDSS DR12 MD-Patchy mocks as a function of the diameter of the balls for 13 sample densities ranging from $5.2 \times 10^{-6} h^3 \mathrm{Mpc}^{-3}$ to $1.7 \times 10^{-4} h^3 \mathrm{Mpc}^{-3}$. Higher density curves lie above lower density ones at small diameters. For the two most extreme densities the plots show as dashed lines the corresponding curves for a Poisson point distribution.

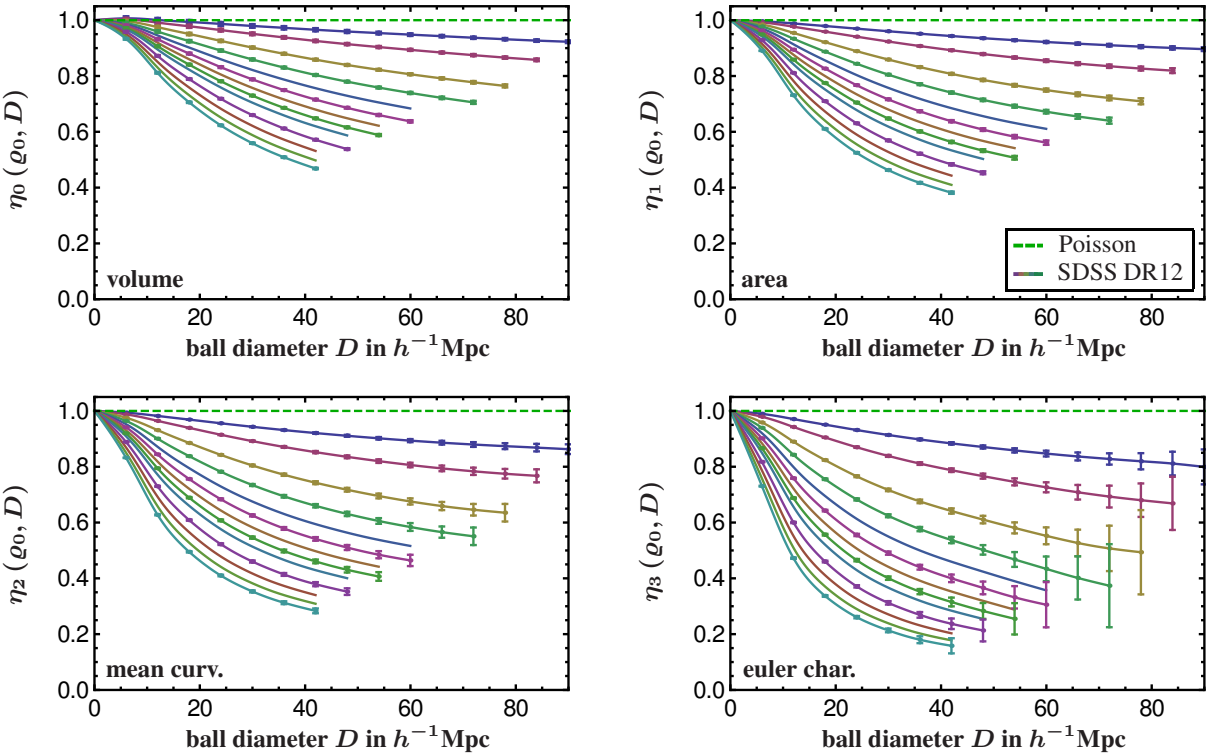

Figure 9. Modified MFs η_μ from Eq. (7) evaluated for 900 SDSS DR12 MD-Patchy mocks and plotted as a function of the diameter of the balls. The lines are the direct transformation of the v_μ-lines of Fig. 8 by Eq. (6). The 13 lines correspond to the same densities as in Fig. 8. High densities lie below low densities. The dashed Poisson line is equal to 1, thanks to the normalization of the η_μ. The η_μ are the quantities that are more directly related to the structure of the sample via the integrated correlation functions of Eq. (7) and that we will therefore use in the following.

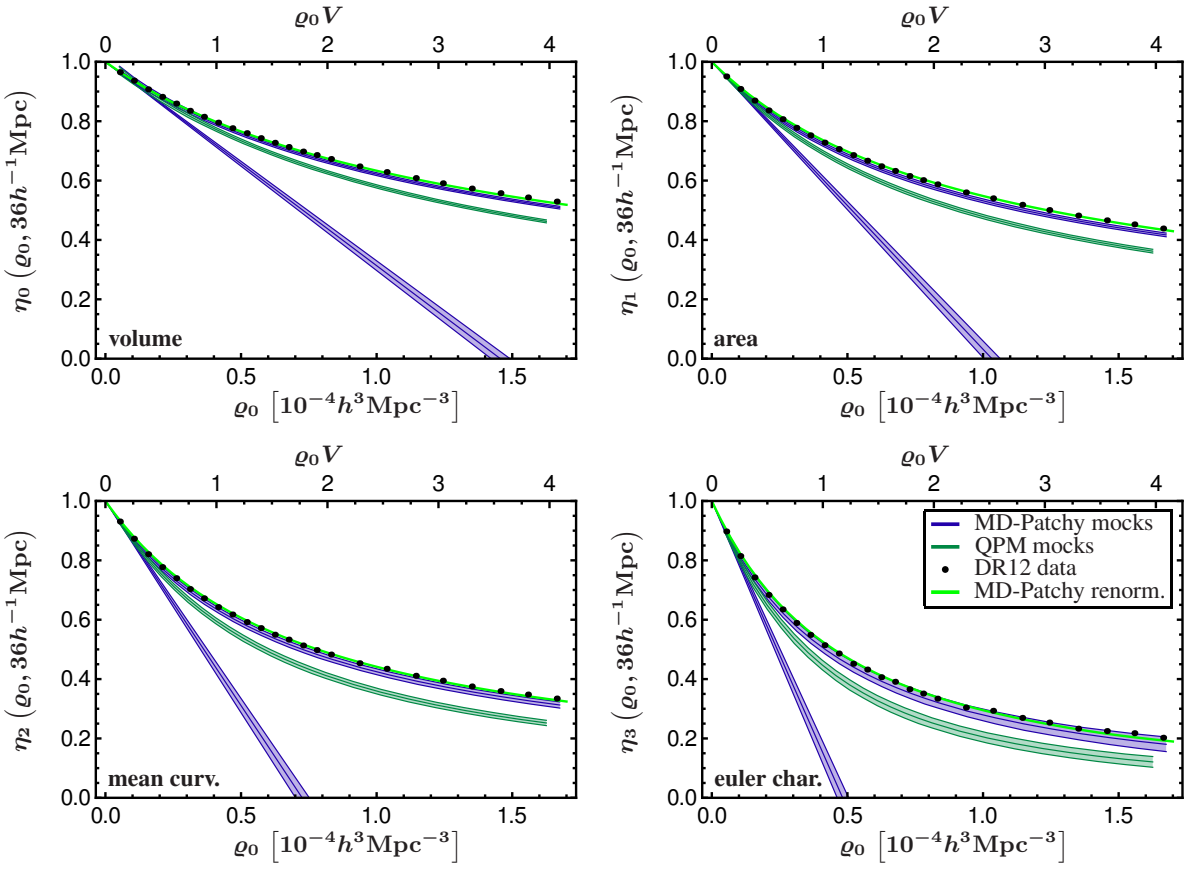

Figure 10. The modified MFs η_μ of Fig. 9, but now as a function of the sampling density for a single diameter of $36h^{-1}\mathrm{Mpc}$. The ϱ_0 parameter direction has the advantage to be simply described by a power series in ϱ_0, see Eq. (8). The curved bands give $1-$ and $2-\sigma$ contours of the 800 QPM (lower, blue band) and 900 MD-Patchy (upper, red band) mocks. For comparison the integrated two-point components derived independently from the same mocks are given by the straight $1-\sigma$ bands. The green line shows the expected change of the average MD-Patchy line for a 5% decrease of σ_8^2.

	QPM $\eta_\mu(\varrho_0)$		MD-P. $\eta_\mu(\varrho_0)$		MD-P. $\eta_\mu^h(\varrho_0)$	
	χ^2	σ_G	χ^2	σ_G	χ^2	σ_G
η_0	1810	41.1	171	10.1	29.8	1.31
η_1	1120	31.7	88.1	5.93	32.1	1.54
η_2	454	19.1	46.9	2.93	29.6	1.28
η_3	182	10.6	29.7	1.30	23.5	0.694

Table 1. Example of χ^2 values for the deviation of the data from the mocks for a single ball diameter of $36h^{-1}\mathrm{Mpc}$. The left table is derived from the full density evolution of η_μ for the QPM mocks (green band compared to black data points in Fig. 10). The central table is the same, but for the MD-Patchy mocks (blue band in Fig. 10). The right table quantifies the deviation of the η_μ^h of the data from the MD-Patchy mocks in Fig. 11. For all tables, χ^2 has 24 degrees of freedom. The tables confirm the results of the figures that the MD-Patchy mocks are describing the data much better than the QPM mocks and that the higher-order MD-Patchy and data part agree quite well at this radius.

4.2 Higher-order correlations in the SDSS galaxy data

We will now turn to the comparison of the density dependence of the modified MFs η_μ in the mocks and in the SDSS data. Instead of probing the grid of Fig. 6 for a fixed density as in Fig. 9, we show in Fig. 10 the η_μ as a function of the sampling density for a ball diameter of $36h^{-1}\mathrm{Mpc}$. The form of η_μ in this direction of parameter space is easier to describe than in the D direction, due to the power series form of the ϱ_0-dependence, see Eq. (8). In the plots of Fig. 10, the Poisson-case corresponds to the horizontal line at 1, thanks to the normalization of the η_μ in Eq. (7). The data are clearly different from 1, showing that there is structure in the galaxy distribution.

The straight lines that depart from the Poisson case at zero density show the η_μ truncated after the term linear in ϱ_0, see Eq. (11). They have been calculated by measuring the two-point correlation functions for each of the 800 QPM and 900 MD-Patchy mocks and integrating them with the corresponding weight functions $V_\mu(R)$ of Eq. (12). The plot shows the average and the $1-\sigma$ fluctuations between the different mock realizations. The average of the correlation functions that formed the basis of these lines is shown in Fig. 7. The clear deviation of the full η_μ of the data and the mocks from these lines shows that the integrals over higher-order correlation functions in the series expansion of η_μ actually do play a significant role for the structure in the SDSS galaxies.

This becomes even more apparent in the plots of Fig. 11. For these we use the integrated two-point correlations and subtract them off the corresponding η_μ for each mock individually. From these subtracted quantities η_μ^h (Eq. (10)) we calculate the mean of

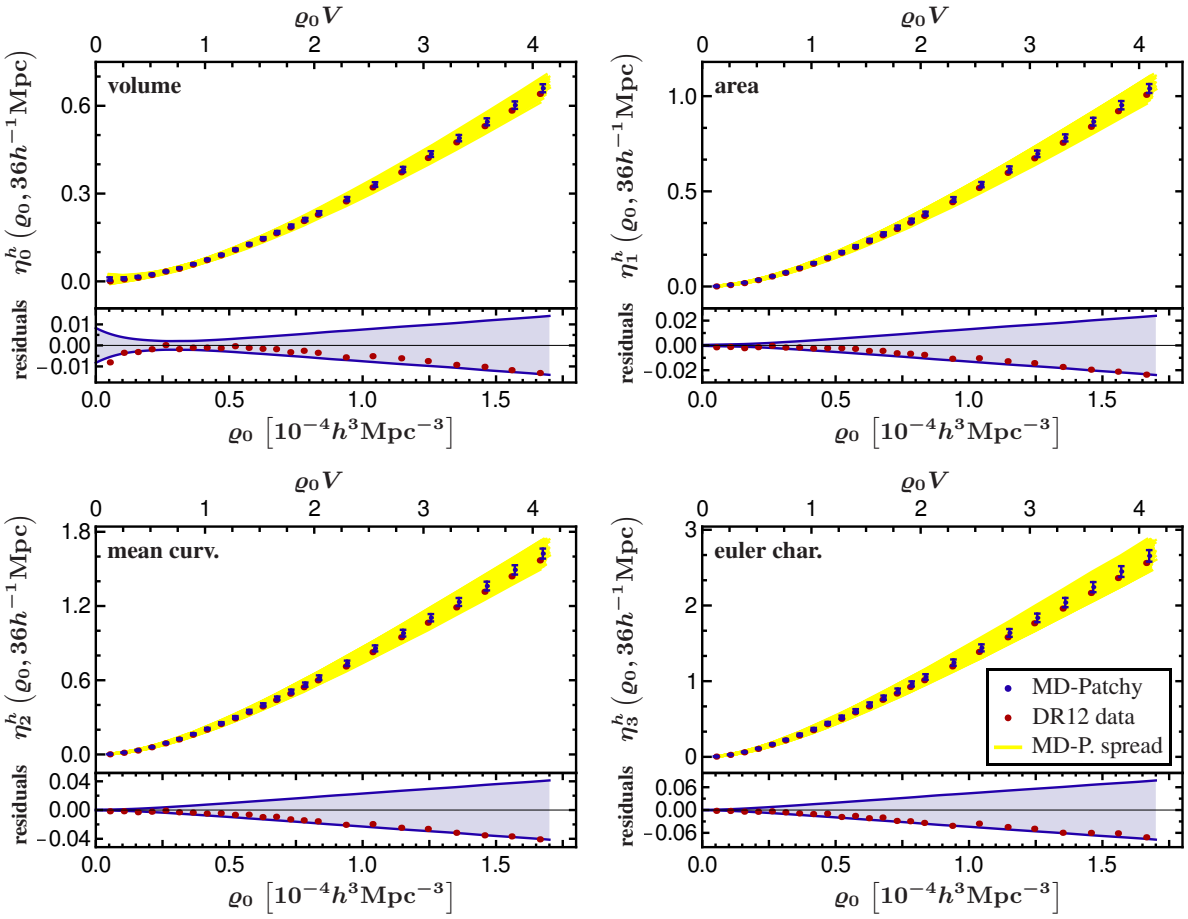

Figure 11. Comparison of the higher-order (3-pt. and higher) part η_μ^h of the MD-Patchy mocks (blue with error bars) with the data (red points) for a ball diameter of $36h^{-1}\mathrm{Mpc}$. This is basically obtained by subtracting the straight two-point lines of Fig. 10 from the curved η_μ lines. The error bars are $1-\sigma$ and the yellow bands show the full spread of the 900 mocks. The lower part of the plots give the residuals of the galaxy data w.r.t. the mean of the mocks. For all four functionals the data happens to be around $1-\sigma$ below the mocks.

	MD-P. $\eta_\mu^h(\varrho_0)$		MD-P. $\eta_\mu^h(\varrho_0)$	
	χ^2	σ_G	χ^2	σ_G
η_0	10300	97.3	290	5.50
η_1	11600	104	282	5.22
η_2	12300	107	221	2.76
η_3	12500	108	252	4.04

Table 2. First column: χ^2 values for the deviation of the higher-order-only η_μ^h of the MD-Patchy mocks in Fig. 11 from the zero line. The value includes all 171 grid points of Fig. 6 between $18h^{-1}\mathrm{Mpc}$ and $66h^{-1}\mathrm{Mpc}$ in diameter. The values indicate a significant contribution of higher-order correlations.
Second column: Combined χ^2 values for the deviation of the SDSS data points in Fig. 11 from the MD-Patchy mocks for the same 171 grid points as the first column.

the mocks and the covariances of the density points. The plots of the residuals show, that the higher-order contributions to the modified MFs are quite well described by the structure in the MD-Patchy mocks. The data happens to lie close to the $1-\sigma$ line of the fluctuations between the 900 mocks for all four MFs. It is quite encouraging that the mocks that were constructed to match the two- and three-point correlations only also capture what is going on in the higher orders quite well.

As the data points in both Fig. 10 and Fig. 11 are strongly correlated, we need to take into account the full covariance matrix in order to estimate the significance of the remaining difference. The results of this calculation are shown in Tab. 1. For the curves of Fig. 10 and Fig. 11 with 24 density points, we first evaluate the χ^2 values and then convert their p-values into those of a two sided deviation for a Gaussian, which we express as multiples of one standard deviation. We inflate the error bars by multiplying the inverse covariance matrix by a factor of $(1 - N_{pts}/N_{mocks})$, in order to account for the finite number of mocks we use for estimating the covariance matrix (Percival et al. 2014). We find that the MD-Patchy mocks are a much better match of the data than the QPM mocks which are about 50σ away from the data in this case. For the higher components only, i.e. the central column of Tab. 1, the agreement is even better and does not exceed 2σ for any of the functionals. So also quantitatively with covariances included the impression from the residual plots of Fig. 11 that the typical deviation is around 1σ is correct.

When we combine all the information of the relevant 171 points in our sampling grid of Fig. 6, i.e. ball diameters from

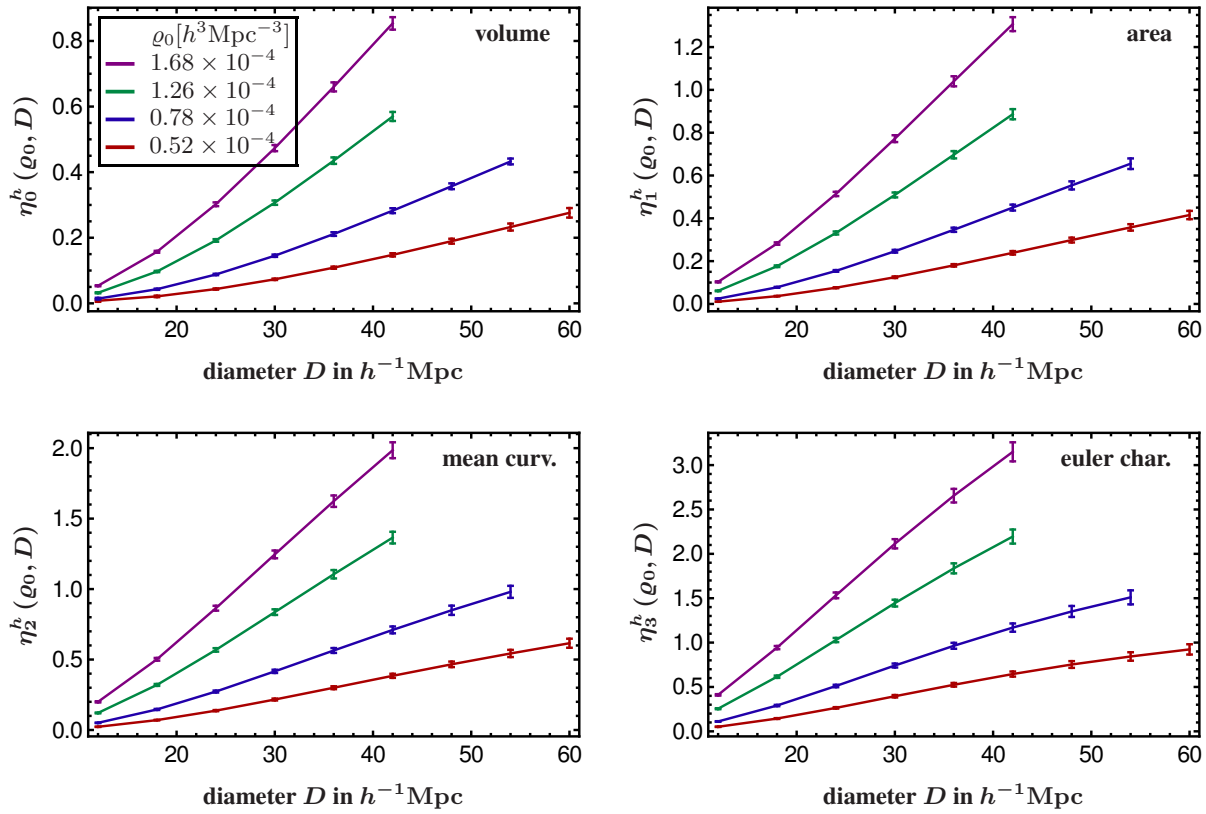

Figure 12. Evolution of the higher-order only part $\eta_\mu^h(\varrho_0, R)$ of Eq. (10) with ball diameter $2R$ for four different densities. The full density dependence for a single diameter of $2R = 36h^{-1}\mathrm{Mpc}$ was shown in Fig. 11. The higher-order signal increases with scale and density.

$18h^{-1}\mathrm{Mpc}$ to $66h^{-1}\mathrm{Mpc}$ and their complete density dependence, we find in Tab. 2 that the deviation of the higher-order MD-Patchy modified MFs is at most 5.5σ. For some diameters as in Tab. 1 the agreement is nearly perfect. This is very encouraging, as the mocks have only been generated to match the two- and three-pt. function. Given the combined values of Tab. 2, it is clear that there is still some room for improvement in the construction of realistic mocks to match the higher orders even better.

Regarding the deviation of the η_μ^h from the case of vanishing higher-order correlations (the zero line in Fig. 11), the conclusion is clear. There is strong evidence for higher-order correlations in the mocks and the data as seen by the MFs. Even though this is not surprising, as at least the three-point function of the SDSS data is well known (see e.g. Slepian et al. (2015) and Gaztañaga et al. (2009); Marín (2011)), it is still interesting to see the statistical power that we have at hand for testing models with different higher-order correlations.

For all of the quantities of Tabs. 1 and 2, one should keep in mind that the different MFs are not independent. So in order to derive one single value that would quantify the mismatch between mocks and data, one would also here have to take the covariances into account. For a single radius this is possible. For the full data set, we are limited by the number of mocks that we analyzed as an estimate of the 684×684 covariance matrix would be noisy.

Finally, let us illustrate the scale dependence of the higher order contributions. Fig. 12 shows the deviation of the full η_μ (7) from the two-point part (11), i.e. η_μ^h of (10). So it is the same quantities as in Fig. 11, but now as a function of ball diameter for four fixed densities $\varrho_0 \in \{0.52, 0.78, 1.26, 1.68\} \times 10^{-4} h^{-1}\mathrm{Mpc}$. The higher the density, the larger is the deviation from the two-point part, because the higher-order contributions play a more important role in the ϱ_0-power series. In the radial direction, the functionals probe the higher-order correlations at different scales. For the two-point part we have seen in Fig. 2 that the integration kernel picks up correlations at larger scales for increasing functional index μ. This is most probably also the case for the higher-order correlations (we explicitly checked it for the three-point integrals) and so η_3^h probes the largest scales that we accessed in this analysis. The decreasing slope of the radial dependence reflects a similar behavior in the three point integral of ξ_3. For even larger scales, the latter integral becomes negative and the difference to the two-point case decreases again.

4.3 Integrated n-point correlation functions

Having found a significant contribution of higher-order correlations to the MFs, we now want to study which orders actually contribute. Using the relation in Eq. (7) we can decompose the functionals in different contributions from higher orders by fitting a polynomial of order n to the density dependence of the η_μ as described in Sec. 2.4. This decomposition is not necessary for using the higher-order MF information in the comparison of the model to the data, as we have shown in the previous section, but it illustrates the convergence properties of the η_μ series.

In Fig. 13 we evaluate the convergence of the fit for increasing polynomial order n. The deviations of the fitted model from the data are quantified in Tab. 3.

From both presentations it is clear that the linear term that only includes the two-point coefficient $c_{\mu,2}$ is a very bad fit to the density evolution. The table indicates that only after the inclusion

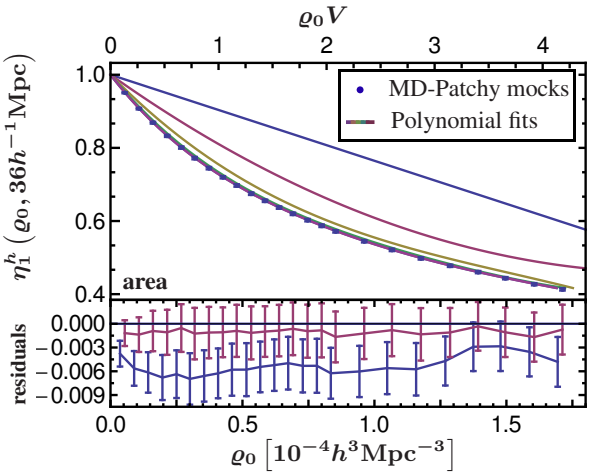

Figure 13. Illustration of the extraction of the fit coefficients $c_{\mu,n}$ of Eq. (9). To the ϱ_0-dependence of η_1 at a diameter of $36h^{-1}\mathrm{Mpc}$ we fit polynomials in ϱ_0 of increasing order taking the full correlations of the points into account and extract the c_μ from the best fit coefficients. The linear to third order polynomials in the large panel give a terrible fit already visually. The fourth and fifth order in the "residual" part of the plot indicate convergence at 5.-order. The corresponding χ^2 values can be found in Tab. 3 and confirm this fact.

fit order	coeff.	χ^2	p-value
1	$c_{1,2}$	7859	10^{-1676}
2	$c_{1,3}$	1509	10^{-306}
3	$c_{1,4}$	306	10^{-52}
4	$c_{1,5}$	47	$6.2 \cdot 10^{-4}$
5	$c_{1,6}$	11.6	$9.7 \cdot 10^{-2}$

Table 3. χ^2 values for the deviation of the best fit polynomial from the ϱ_0-dependence of η_1 for the mean of 900 MD-Patchy mocks at a ball diameter of $36h^{-1}\mathrm{Mpc}$. The corresponding curves are shown in Fig. 13. There are 24 points to fit. Only after adding the fifth coefficient, corresponding to the 6-point function integral, to the fit, the χ^2 values become acceptable.

of the fifth term, which corresponds to integrals over the six-point function, the polynomial fit captures the shape of the modified MFs well. However, this only means that we have some sensitivity of the MFs of the mocks to contributions from up to the six-point function. It does not mean that these contributions are also significantly different from the ones in the data. In fact, as we have found in Sec. 4.2 the higher-order contributions of the mocks and the data actually agree relatively well.

In order to evaluate how strongly the coefficients $c_{\mu,n}$ of Eq. (8) are biased by truncating the power series at a finite n, we plot in Fig. 14 the dependence of the mean of the best fit values of $c_{1,2}$, $c_{1,3}$ and $c_{1,4}$ of the 900 MD-Patchy mocks on the polynomial order n for a fit at a diameter of $36h^{-1}\mathrm{Mpc}$. As high values of n also increase the chance of picking up spurious fluctuations, we decided to put a prior on the higher order coefficients. To this end we fit a three-parameter Padé model to the density evolution of the mean MFs extracted from 100 periodic MD-Patchy cubes. Taylor expanding this model provides some model for the higher-order coefficients. We choose a Gaussian prior around the so obtained values with a standard deviation corresponding to the value of the mean $G\left(\mu, \sigma = \mu\right)$. We only apply this prior to coefficients beyond the four-point function coefficient $c_{\mu,4}$. The first two coefficients $c_{\mu,2}$ and $c_{\mu,3}$ are already well measured without any prior, and for $c_{\mu,4}$ it is sufficient to regularize the higher orders. Fig. 14 shows that the value of the first coefficient $c_{\mu,2}$ is independent of n as soon as n is high enough that we have a good fit, i.e. $n = 5$ from Fig. 13. The second coefficient $c_{\mu,3}$ is also largely independent of fit order, but needs a higher fit order n than $c_{\mu,2}$ to be unbiased. For $c_{\mu,4}$ there is still some remaining uncertainty from the fit order, which is, however, still much smaller than the error from the scatter of the mocks.

Fig. 15 shows evolution of the mean value together with the $1-\sigma$ contours of the parameters $c_{1,3}$ and $c_{1,4}$ for different n starting at $n = 3$, to include also the covariances between the parameters. Below the order 5 that provides the first good fit in Tab. 3, the best fit values are strongly dependent on fit order. For orders starting at $n = 9$ the shift becomes much smaller than the scatter of the mocks. For the following plots, we will use polynomials of order 9 for the η_1 fit at $D = 36h^{-1}\mathrm{Mpc}$. To determine the fit order for the radii with a smaller number of density points, i.e. beyond $42h^{-1}\mathrm{Mpc}$, we constructed and analyzed test data. These were created from a Padé model fit to the cut sky mocks and provide a model with known coefficients. Then we applied the fitting procedure to these test data and found that for high enough n, the coefficients we put in were recovered within the errors estimated by the fluctuations from the mocks. From the results of these test data fits, we determined for every diameter the minimum n needed. For the larger diameters this value is lower due to the decreasing contribution of higher orders. The reason for this decrease is the steep scale dependence for the higher-order coefficients, an example of which we will see in Fig. 17 for the three-point term (see also Fig. 14 of Wiegand et al. (2014) for the scale dependence of the coefficients of η_0 for a Log-Normal model).

The decomposition into n-point components also allows us to test to which extent the deviation of the data from the mocks in Fig. 10 could be simply the result of a misnormalization of the power spectrum. The green line in Fig. 10 therefore shows the mean of the MD-Patchy mocks for a reduction in the power of 5%. It has been obtained by taking the coefficients of the 6-th order fit of Fig. 13 and multiplying the integrated correlation functions with the power of the reduction factor that corresponds to the number of power spectra involved, i.e. 0.95^n for ξ_{n+1}. Of course this is only a very simplified model, given that the fit is not unbiased, especially for higher orders, but it should still provide a useful approximation. From the result in Fig. 13 we see that at least approximately it removes the offset of the data from the mocks and makes them agree even better. This seems to be consistent with the analysis of the power spectrum in Beutler et al. (2016). Our redshift range roughly corresponds to their second redshift bin, for which their Fig. 1 indicates that the data also is slightly lower than the mean of the MD-Patchy mocks.

For the two cases $c_{\mu,2}$ and $c_{\mu,3}$ where the convergence in Fig. 14 is convincing, we compare in Figs. 16 and 17 the extracted coefficients to reference models. Fig. 16 shows the two-point coefficients $c_{\mu,2}$. For those, $c_{0,2}$ coincides with $\sigma^2\left(R\right)$ (see Eq. (13)) and $c_{3,2}$ corresponds to the volume averaged correlation function (see Eq. (14)). In addition to the average of the coefficients extracted from the MD-Patchy mocks, we show the coefficients of the data and the expected coefficients derived from integrals over the average two-point correlation function that we measured independently. The overall agreement of the two independent determinations is reassuring. It provides a confirmation that the fit to $\eta_\mu\left(\varrho_0\right)$

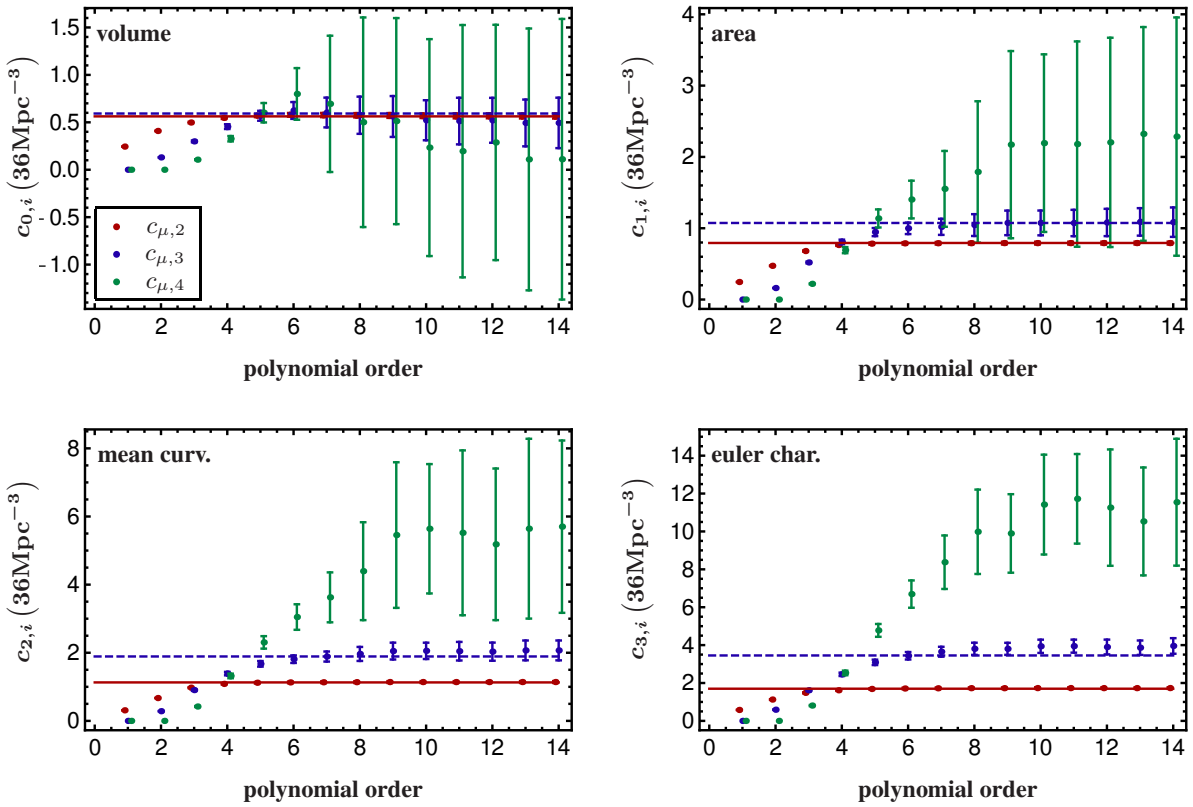

Figure 14. Evolution of the best fit value of the first three coefficients $c_{\mu,n+1}$ of Eq. (9) with fit order n for a ball diameter of $36h^{-1}\mathrm{Mpc}$. $c_{\mu,2} < c_{\mu,3} < c_{\mu,4}$ for large n. The solid (red) lines are the coefficients calculated from the two-point integrals of our measurement of the correlation function. The dashed (blue) lines are the predictions from the integral over the model three-point correlation function of Slepian & Eisenstein (2016) with $b_1 = 2.19$, $b_2 = 0$ and $b_t = -0.34$.

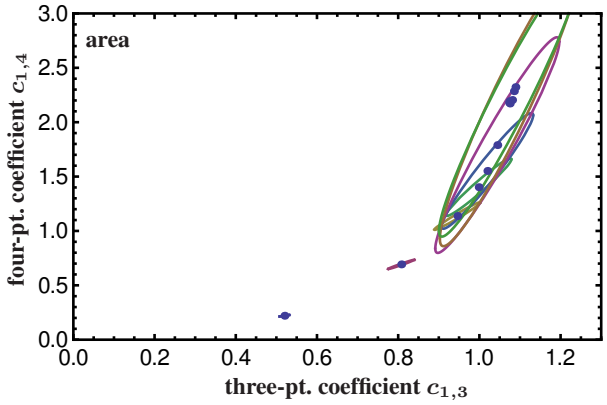

Figure 15. Evolution of the best fit coefficients $c_{1,3}$ and $c_{1,4}$ of the fit to $\eta_1\,(\varrho_0)$ of Fig. 13 for a diameter of $36h^{-1}\mathrm{Mpc}$. The leftmost point is for a third order polynomial and the order is increasing from left to right with a maximum order of 14. The error bars indicate $1-\sigma$ intervals. Starting from the ninth order, error bars include all higher order points.

can extract individual terms from the power series (7). There is, however, for some of the functionals a relatively large offset. It is not clear if this offset is due to residual bias in the fitting method, or if our method to estimate the correlation function of a mock does not include the boundaries in the same way than the MFs.

Fig. 17 then shows the $c_{\mu,3}$. The connection to other known quantities is not as apparent as in the two-point case and we did not obtain an independent estimate of the three-point correlation integrals. What is shown in Fig. 17 instead is the three-point function model of Slepian & Eisenstein (2016). It is based on leading-order perturbation theory and includes redshift space distortions. For the plots in Fig. 17 we fixed the three bias parameters to $b_1 = 2.19$, $b_2 = 0$ and $b_t = -0.34$. The b_1-value is the one we used in Fig. 16 and the b_t-value is obtained from Eq. (23) in Slepian & Eisenstein (2016) and based on local Lagrangian biasing (Baldauf et al. 2012; Chan et al. 2012). We did not attempt to fit for b_2 and so the lines in Fig. 17 do not contain any free parameter. Given that, the match of the model with the extracted coefficients is encouraging.

4.4 The occurrence of large voids

In addition to being related to the hierarchy of n-point correlation functions, the MFs also contain information about the cosmic web. For example, the partial functionals probe the local morphology around the galaxy sites, and for an isodensity contour smoothing "shapefinders" have been defined to quantify the amount of filamentary vs. planarity of the local density field (Sahni et al. 1998; Schmalzing et al. 1999; Schmalzing 1999).

For the global germ-grain MF densities that we study here, there are different quantities that can be extracted. The Euler characteristic $\chi = v_3 V$, for example, indicates for large balls how many extreme voids (i.e. regions that are further away from any galaxy than $2R_{max}$) there are in the galaxy distribution. The area functional v_1 gives an idea of their area and v_0 their volume. More generally, the comparison of the void fraction $1 - v_0$ to the one of a

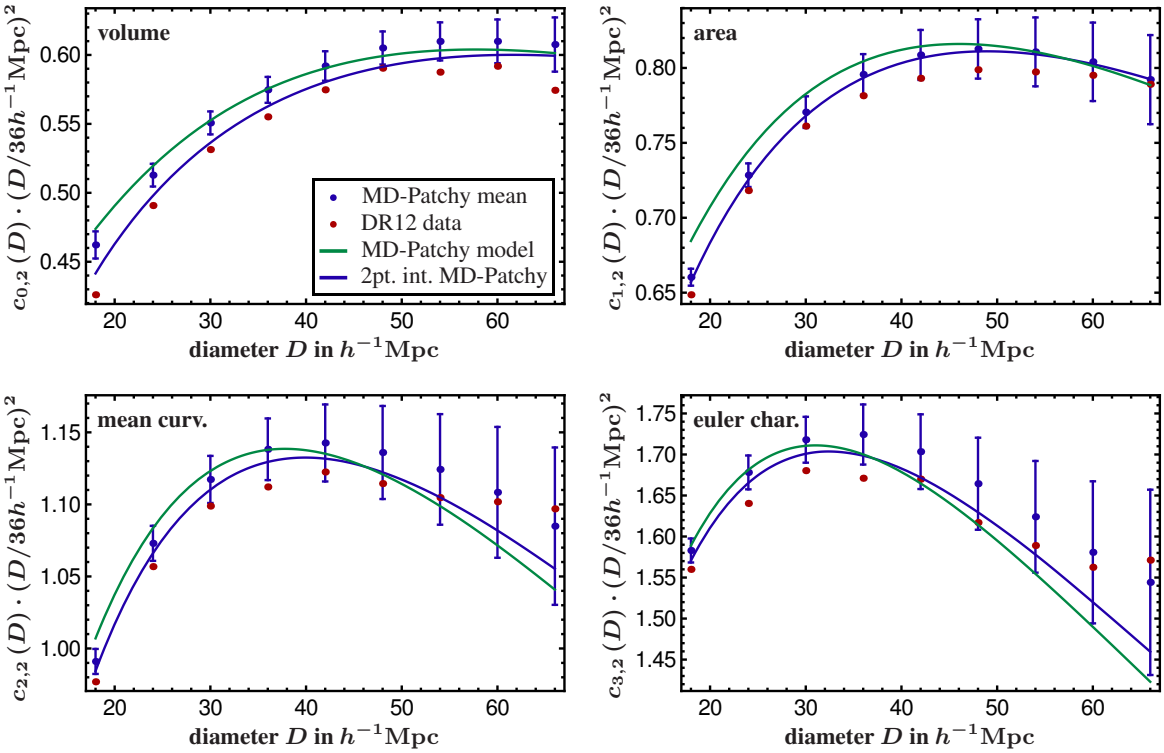

Figure 16. Linear term of the ϱ_0-series Eq. (8) for the MD-Patchy mocks and the DR12 galaxy data. The linear coefficient corresponds to the integrated two-point correlation function of Eq. (9). It is obtained by fitting a polynomial to the density dependence of the η_μ for different ball diameters. The fit is illustrated in Fig. 13. The blue solid line is the corresponding integral determined from an independent measurement of the two-point correlation function. The green line is the integral of the non-linear MD-Patchy power spectrum at $z = 0.50$ with a linear bias of $b_1 = 2.19$.

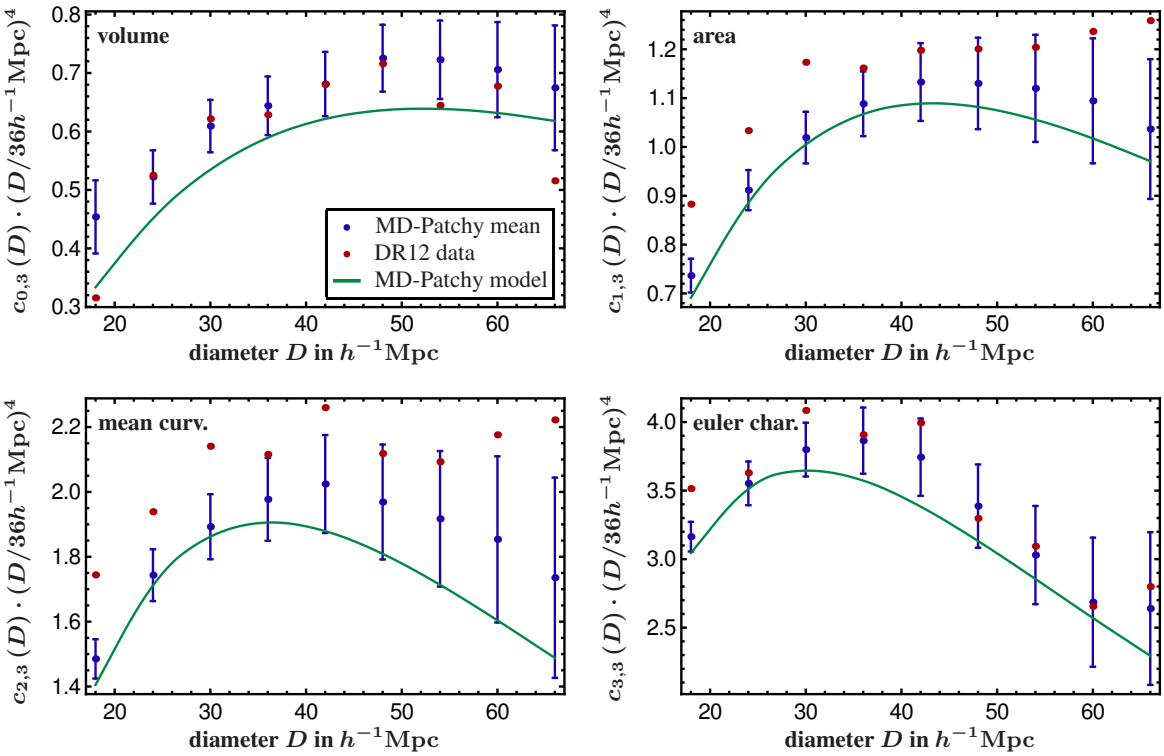

Figure 17. Quadratic term of the ϱ_0-series Eq. (8) for the MD-Patchy mocks and the DR12 galaxy data. This quadratic coefficient corresponds to the integrated three-point correlation function of Eq. (9). The result is from the same fit as Fig. 16. The solid line is the integral over the model three-point correlation function of Slepian & Eisenstein (2016) with $b_1 = 2.19$ as above, $b_2 = 0$ and $b_t = -0.34$.

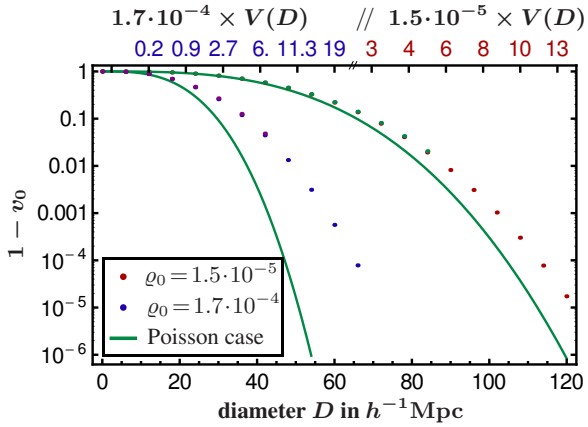

Figure 18. Fraction of unfilled volume for two different sample densities as a function of the ball radius. The top scale gives the corresponding $\varrho V(D)$ for a ball of diameter D, where the first values correspond to the lower (blue) points and the values restarting at 3 to the upper (red) points. The densities are $\varrho_1 = 1.68 \times 10^{-4} h^3\mathrm{Mpc}^{-3}$ and $\varrho_{24} = 1.54 \times 10^{-5} h^3\mathrm{Mpc}^{-3}$. Especially for the higher density the solid Poisson lines lie way below the values for the data, so the structure leads to a significantly higher void fraction than we would expect in an unclustered field.

Poisson distribution of the same density indicates how inhomogeneously these void regions are distributed.

In Fig. 18, we therefore show $1 - v_0$ as a function of the ball diameter and compare it to the corresponding Poisson case. Especially for the higher density of $\varrho_1 = 1.68 \times 10^{-4} h^3\mathrm{Mpc}^{-3}$ the difference is quite remarkable. For a diameter of $42h^{-1}\mathrm{Mpc}$, the volume is a factor of ≈ 30 larger than in the Poisson case. For the most extreme case of $66h^{-1}\mathrm{Mpc}$, it is nearly 10^7. In this latter case the expected number of galaxies in a ball of diameter $66h^{-1}\mathrm{Mpc}$ would be 25. With the standard Poisson fluctuation one would expect a fraction of $\approx 10^{-11}$ to be uncovered. Including the observed structure however, there is $\approx 8 \times 10^{-5}$ of the $1.38h^{-3}\mathrm{Gpc}^3$ in our analyzed region that remain uncovered.

Of course one has to make sure that this conclusion is not significantly affected by the holes in the survey. We tested this using the periodic cubic MD-Patchy mocks and plot the resulting void fractions as purple and green points in Fig. 18. For the region that we evaluated, the cubic mocks for the difference is small, below 4% for ϱ_1 and below 9% for ϱ_{24}. However, for the more extreme diameters the deviations will grow, but we do not expect that this affects the general picture.

5 CONCLUSION

In this paper, we perform a new analysis that combines Minkowski Functionals with the standard two-point correlation function to measure the amount of non-Gaussianity of the density field. We find in Sec. 4.2 that the significance of the higher-order contribution to the MFs is of the order of 100σ (see Tab. 2 and Fig. 11). This demonstrates that this part of the MFs can be well enough measured to give meaningful constraints on the higher-order properties of the galaxy distribution.

Given this constraining power it is reassuring that we find from Fig. 11 and Tab. 1 that the MD-Patchy mocks, that were constructed to match the two- and three-point properties of the measured galaxy distribution, match fairly well to the higher-order MFs. This indicates that as far as the higher-orders accessible by the MFs are concerned, the mock galaxy catalogs are quite good. There is still some room for improvement as the combined deviation is as large as 5σ for some functionals (see Tab. 2), but this might be addressed by a 5% shift in the normalization of the mock power spectrum (see Fig. 10).

On the technical side, our careful boundary treatment minimizes the effects of the survey geometry on our measurement of the modified MFs (see Fig. 4). The corrected values lie within the error bars of a boundaryless periodic box.

For the QPM mocks, we find a much larger deviation (beyond 10σ) from the data than for MD-Patchy (see Tab. 1). As in this case already the two-point correlations are overnormalized in the range of scales that we are interested in (see Fig. 7), a reduction of the amplitude of the initial Gaussian field could also help in this case.

We show that in the the higher-order part of the MFs calculated for the SDSS DR12 CMASS galaxies contains at least information up to the integrated 6-point function (see Tab. 3). This underlines the power of the MFs to bring condensed higher-order information into a simple functional form.

Acknowledgements

AW thanks Antonio Cuesta for providing support with the QPM correlation functions. We thank Graziano Rossi and Thomas Buchert for valuable comments on the manuscript. The work of AW was supported by the German research organization DFG, Grant No. WI 4501/1-1. DJE is supported by U.S. Department of Energy grant DE-SC0013718 and as a Simons Foundation Investigator.

Funding for SDSS-III has been provided by the Alfred P. Sloan Foundation, the Participating Institutions, the National Science Foundation, and the U.S. Department of Energy Office of Science. The SDSS-III web site is http://www.sdss3.org/.

SDSS-III is managed by the Astrophysical Research Consortium for the Participating Institutions of the SDSS-III Collaboration including the University of Arizona, the Brazilian Participation Group, Brookhaven National Laboratory, Carnegie Mellon University, University of Florida, the French Participation Group, the German Participation Group, Harvard University, the Instituto de Astrofisica de Canarias, the Michigan State/Notre Dame/JINA Participation Group, Johns Hopkins University, Lawrence Berkeley National Laboratory, Max Planck Institute for Astrophysics, Max Planck Institute for Extraterrestrial Physics, New Mexico State University, New York University, Ohio State University, Pennsylvania State University, University of Portsmouth, Princeton University, the Spanish Participation Group, University of Tokyo, University of Utah, Vanderbilt University, University of Virginia, University of Washington, and Yale University.

References

Aihara H. et al., 2011, APJS, 193, 29, 1101.1559, ADS
Alam S. et al., 2015, APJS, 219, 12, 1501.00963, ADS
Alam S. et al., 2016, ArXiv e-prints, 1607.03155, ADS
Aragon-Calvo M. A., Shandarin S. F., Szalay A. 2010, ArXiv e-prints, 1006.4178, ADS
Baldauf T., Seljak U., Desjacques V., McDonald P. 2012, PRD, 86, 083540, 1201.4827, ADS
Beutler F. et al., 2016, ArXiv e-prints, 1607.03149, ADS
Blake C., James J. B., Poole G. B. 2014, MNRAS, 437, 2488, 1310.6810, ADS
Bolton A. S. et al., 2012, AJ, 144, 144, 1207.7326, ADS

Buchert T., 1995, in Mücket J. P., Gottlöber S., Müller V., eds, Large Scale Structure in the Universe Robust Morphological Measures for Large Scale Structure. p. 156, astro-ph/9412061, ADS
Chan K. C., Scoccimarro R., Sheth R. K. 2012, PRD, 85, 083509, 1201.3614, ADS
Choi Y.-Y. et al., 2013, APJS, 209, 19, 1309.4381, ADS
Codis S. et al., 2013, MNRAS, 435, 531, 1305.7402, ADS
Cuesta A. J. et al., 2016, MNRAS, 457, 1770, 1509.06371, ADS
Dawson K. S. et al., 2016, AJ, 151, 44, 1508.04473, ADS
Dawson K. S. et al., 2013, AJ, 145, 10, 1208.0022, ADS
Doi M. et al., 2010, AJ, 139, 1628, 1002.3701, ADS
Ducout A. et al., 2013, MNRAS, 429, 2104, 1209.1223, ADS
Einasto M. et al., 2014, A&A, 562, A87, 1401.3226, ADS
Eisenstein D. J. et al., 2011, AJ, 142, 72, 1101.1529, ADS
Fry J. N., Peebles P. J. E. 1978, ApJ, 221, 19, ADS
Fukugita M. et al., 1996, AJ, 111, 1748, ADS
Gaztañaga E. et al., 2009, MNRAS, 399, 801, 0807.2448, ADS
Gleser L., Nusser A., Ciardi B., Desjacques V. 2006, MNRAS, 370, 1329, astro-ph/0602616, ADS
Gunn J. E. et al., 1998, AJ, 116, 3040, astro-ph/9809085, ADS
Gunn J. E. et al., 2006, AJ, 131, 2332, astro-ph/0602326, ADS
Hadwiger H., 1957, Vorlesungen über Inhalt, Oberfläche und Isoperimetrie. Die Grundlehren der mathematischen Wissenschaften in Einzeldarstellungen mit besonderer Berücksichtigung der Anwendungsgebiete ; 93, Springer, ISBN: 3-540-02151-5,
Hikage C., Matsubara T. 2012, MNRAS, 425, 2187, 1207.1183, ADS
Hikage C. et al., 2003, PASJ, 55, 911, astro-ph/0304455, ADS
Kerscher M., 2001, PRE, 64, 056109, astro-ph/0102153, ADS
Kerscher M. et al., 2001, A&A, 373, 1, astro-ph/0101238, ADS
Kerscher M., Schmalzing J., Buchert T., Wagner H. 1996, in Weiss A., Raffelt G., Hillebrandt W., von Feilitzsch F., Buchert T., eds, Astro-Particle Physics The significance of the fluctuations in the IRAS 1.2 Jy galaxy catalogue.. pp 83–98, ADS
Kerscher M., Schmalzing J., Buchert T., Wagner H. 1998, A&A, 333, 1, astro-ph/9704028, ADS
Kerscher M. et al., 1997, MNRAS, 284, 73, astro-ph/9606133, ADS
Kerscher M., Szapudi I., Szalay A. S. 2000, ApJ, 535, L13, astro-ph/9912088, ADS
Kitaura F.-S. et al., 2016, MNRAS, 456, 4156, 1509.06400, ADS
Kitaura F.-S., Yepes G., Prada F. 2014, MNRAS, 439, L21, 1307.3285, ADS
Kratochvil J. M. et al., 2012, PRD, 85, 103513, 1109.6334, ADS
Laureijs R. et al., 2011, ArXiv e-prints, 1110.3193, ADS
Levi M. et al., 2013, ArXiv e-prints, 1308.0847, ADS
Lupton R. et al., 2001, in Harnden Jr. F. R., Primini F. A., Payne H. E., eds, Astronomical Data Analysis Software and Systems X Vol. 238 of Astronomical Society of the Pacific Conference Series, The SDSS Imaging Pipelines. p. 269, astro-ph/0101420, ADS
Marín F., 2011, ApJ, 737, 97, 1011.4530, ADS
Marín F. A. et al., 2013, MNRAS, 432, 2654, 1303.6644, ADS
Mecke K., Wagner H. 1991, Journal of Statistical Physics, 64, 843
Mecke K. R., Buchert T., Wagner H. 1994, A&A, 288, 697, astro-ph/9312028, ADS
Modest H. I. et al., 2013, MNRAS, 428, 551, 1209.5106, ADS
Munshi D. et al., 2013, MNRAS, 434, 2830, 1011.5224, ADS
Nakagami T., Matsubara T., Schmalzing J., Jing Y. 2004, ArXiv Astrophysics e-prints, astro-ph/0408428, ADS
Neyrinck M. C., Szapudi I., Szalay A. S. 2009, ApJ, 698, L90, 0903.4693, ADS
Neyrinck M. C. et al., 2011, in American Astronomical Society Meeting Abstracts #218 The Log-Density as a Better Cosmological Density Variable. p. #233.04, ADS
Padmanabhan N. et al., 2008, ApJ, 674, 1217, astro-ph/0703454, ADS
Peebles P. J. E., Groth E. J. 1975, ApJ, 196, 1, ADS
Percival W. J. et al., 2014, MNRAS, 439, 2531, 1312.4841, ADS
Petri A. et al., 2013, PRD, 88, 123002, 1309.4460, ADS
Pier J. R. et al., 2003, AJ, 125, 1559, astro-ph/0211375, ADS
Planck Collaboration XVI, 2016, A&A, 594, A16, 1506.07135, ADS
Planck Collaboration XXIII, 2014a, A&A, 571, A23, 1303.5083, ADS
Planck Collaboration XXV, 2014b, A&A, 571, A25, 1303.5085, ADS
Platzöder M., Buchert T. 1996, in Weiss A., Raffelt G., Hillebrandt W., von Feilitzsch F., Buchert T., eds, Astro-Particle Physics Applications of Minkowski-Functionals to the Statistical Analysis of Dark Matter Models. p. 251, astro-ph/9509014, ADS
Pratten G., Munshi D. 2012, MNRAS, 423, 3209, 1108.1985, ADS
Reid B. et al., 2016, MNRAS, 455, 1553, 1509.06529, ADS
Sahni V., Sathyaprakash B. S., Shandarin S. F. 1998, ApJ, 495, L5, astro-ph/9801053, ADS
Sathyaprakash B. S., Sahni V., Shandarin S. 1998, ApJ, 508, 551, astro-ph/9805285, ADS
Schmalzing J., 1999, PhD thesis, LMU München
Schmalzing J., Buchert T. 1997, ApJ, 482, L1, astro-ph/9702130, ADS
Schmalzing J. et al., 1999, ApJ, 526, 568, astro-ph/9904384, ADS
Schmalzing J., Gorski K. M. 1998, MNRAS, 297, 355, astro-ph/9710185, ADS
Schmalzing J., Gottlöber S., Klypin A. A., Kravtsov A. V. 1999, MNRAS, 309, 1007, astro-ph/9906475, ADS
Schmalzing J., Kerscher M., Buchert T. 1996, in Bonometto S., Primack J. R., Provenzale A., eds, Dark Matter in the Universe Minkowski Functionals in Cosmology. p. 281, astro-ph/9508154, ADS
Schmalzing J., Takada M., Futamase T. 2000, ApJ, 544, L83, ADS
Slepian Z., Eisenstein D. J. 2015, MNRAS, 448, 9, 1411.4052, ADS
Slepian Z., Eisenstein D. J. 2016, ArXiv e-prints, 1607.03109, ADS
Slepian Z. et al., 2015, ArXiv e-prints, 1512.02231, ADS
Smee S. A. et al., 2013, AJ, 146, 32, 1208.2233, ADS
Smith J. A. et al., 2002, AJ, 123, 2121, astro-ph/0201143, ADS
Stratonovich R. L., 1963, Topics in the theory of random noise. Vol. Vol. 1, Gordon and Breach, New York
Wang X. et al., 2011, ApJ, 735, 32, 1103.2166, ADS
White M., Tinker J. L., McBride C. K. 2014, MNRAS, 437, 2594, 1309.5532, ADS
White S. D. M., 1979, MNRAS, 186, 145, ADS
Wiegand A., Buchert T., Ostermann M. 2014, MNRAS, 443, 241, 1311.3661, ADS
York D. G. et al., 2000, AJ, 120, 1579, astro-ph/0006396, ADS
Yoshiura S., Shimabukuro H., Takahashi K., Matsubara T. 2016, ArXiv e-prints, 1602.02351, ADS

This paper has been typeset from a TEX/LATEX file prepared by the author.